Department of Complexity Science and Engineering

Graduate School of Frontier Sciences

The University of Tokyo

2024

Master Thesis

Effects of Laboratory-Simulated Space Weathering on the UV Spectra of Polycyclic Aromatic Hydrocarbons (PAHs)

Submitted August 30, 2024

Adviser: Professor Ichiro Yoshikawa

劉 姝玥

Shuyue Liu

Abstract

Polycyclic aromatic hydrocarbons (PAHs) are ubiquitous organic molecules commonly present in various astrophysical environments, including the interstellar medium (ISM) and carbonaceous chondrites, where they undergo several weathering processes. They are also considered to be the building blocks of life. The theoretical hypothesis suggests that the absorption peak of PAHs in the ultraviolet region may correspond to the 217.5 nm absorption peak in the ISM extinction curve. Space weathering refers to the process by which objects are exposed to the harsh environment of outer space, experiencing grain-grain collisions and irradiation, affecting their physical and optical properties, potentially shifting absorption peaks.

In this study, UV irradiation was used to simulate space weathering. In a vacuum environment, two different light sources were employed to irradiate PAH samples: a deuterium arc lamp and the 0th-order light from the synchrotron radiation source UVSOR. Two kinds of PAH samples, coronene and anthracene, were used. During the irradiation process, the vacuum system was connected to a Quadrupole Mass Spectrometer (QMS) to analyze substances produced or fragmented during irradiation. Subsequently, we measured the UV spectra of both the unirradiated control group and the experimental groups exposed to different durations and light sources using the BL7B beamline at UVSOR, analyzing any observed changes.

The primary findings include the observation of fragmentation and evaporation of anthracene during irradiation, with anthracene showing a higher tendency for photodissociation under the deuterium arc lamp. In contrast, coronene, being a larger and more stable PAH, did not exhibit significant decomposition under UV irradiation. Both anthracene and coronene samples, when compared between irradiated and non-irradiated groups, displayed a tendency for the UV absorption peaks to shift towards shorter wavelengths post-irradiation.

These results enhance the understanding of space weathering processes that alter the chemistry and structure of PAHs and their influence on absorption peaks, contributing to a deeper comprehension of the interstellar medium's composition and dynamics.

Keyword: PAH, anthracene, coronene, space weathering, UV-Vis Spectroscopy, UV irradiation, Mass Spectroscopy

Contents

1. Introduction

1.1. Background

1.1.1 Polycyclic Aromatic Hydrocarbons (PAHs)

Polycyclic aromatic hydrocarbons (PAHs) are ubiquitous organic molecules commonly found in various astrophysical environments, such as the interstellar medium and carbonaceous chondrites, where they undergo various weathering processes. These molecules are also considered fundamental building blocks of life.

PAHs are composed of multiple fused benzene rings, forming a planar, conjugated structure. These molecules consist solely of carbon and hydrogen atoms, with carbon atoms typically forming a hexagonal lattice. PAHs can vary in size and complexity, ranging from small molecules like naphthalene (two rings) to larger structures with many fused rings like fullerene.

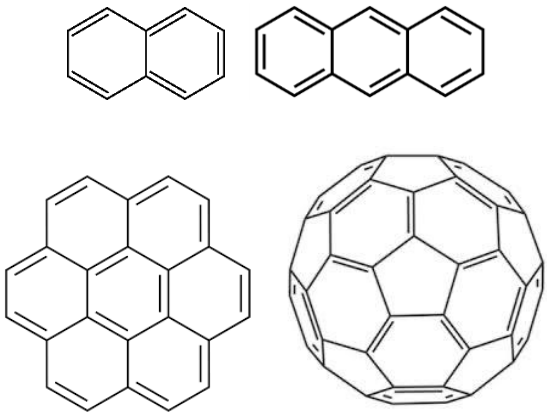

Figure 1.1.1 Common PAH molecules

(Upper Left to Right: Naphthalene $C_{10}H_8$, Anthracene $C_{14}H_{10}$.

Lower Left to Right: Coronene $C_{24}H_{12}$, Fullerene C_{60}.)

1.1.2 Interstellar Medium and Extinction Curve

The interstellar medium (ISM) is the space between star systems in a galaxy, consisting of gas and dust. Dust in the ISM causes extinction, where electromagnetic radiation is absorbed and scattered as it passes through the medium. The extinction curve, which

varies with particle composition and size distribution, is crucial for understanding dust properties.

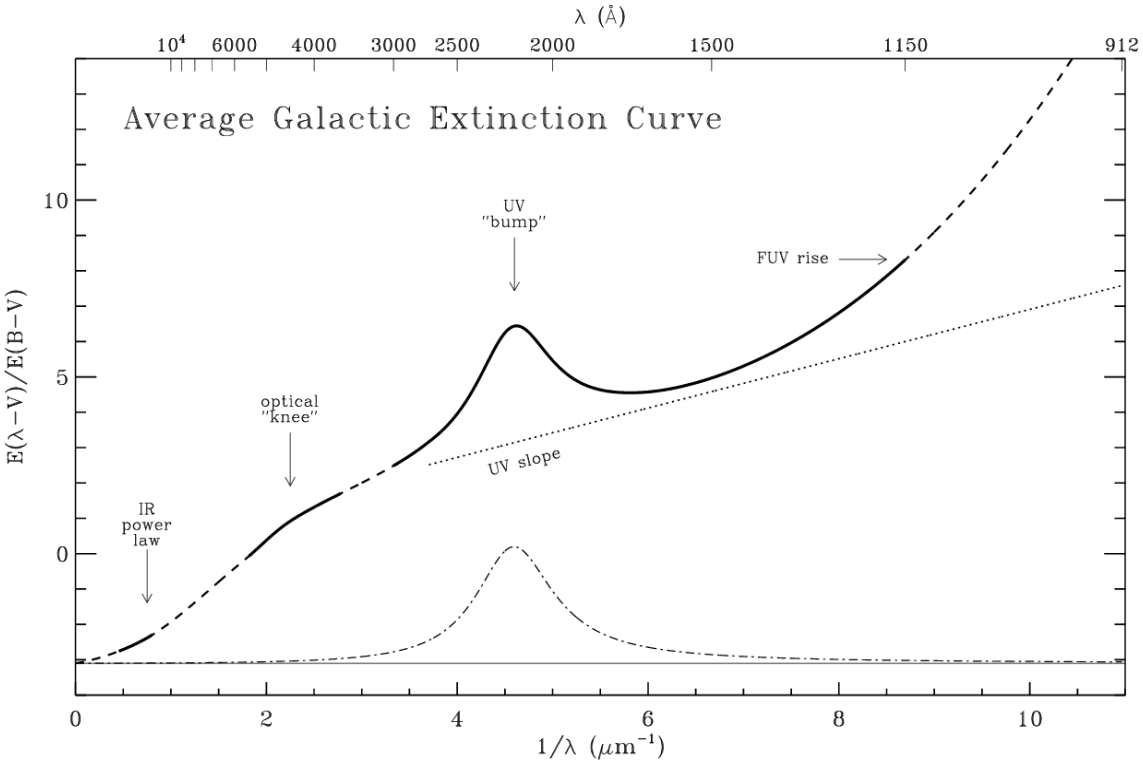

Figure 1.1.2 Average Galactic Extinction Curve in the Milky Way galaxy (Fitzpatrick, 2004)

The most prominent feature in the interstellar extinction curve is the ultraviolet (UV) "bump" at 217.5 nm, commonly referred to as the 220 nm feature (Stecher, 1965). The UV bump is potentially carried by several proposed candidates, including graphite grains (e.g., Mathis et al., 1977; Mathis, 1987; Ferriere, 2001), hydrogenated amorphous carbon, and core particles (such as silicates or graphite) coated with a PAH mantle (e.g., Henning and Schnaiter, 1998). Many PAHs are showing an absorption peak near 200 nm, which is due to their π-π* electronic transitions. And these peaks may produce a broad absorption band resembling to the 217.5 nm UV bump (Steglich et al. 2010)

PAHs are significant constituents of the interstellar medium (ISM), containing ≲20% of the carbon in ISM by analyzing observation data (Tielens, 2013). They are prevalent in the ISM and meteorites, and are also found in the samples of Ryugu (Zeichner et al.,

2023). PAHs undergo photodissociation(carbon or hydrogen loss) and hydrogenation, potentially leading to the formation of fullerenes under specific conditions, even in hydrogen-rich environments (Murga et al., 2022). Furthermore, PAHs demonstrate growth pathways at low temperatures and experience fragmentation under UV radiation, contributing to the synthesis of complex hydrocarbons in UV-rich regions (Banhatti et al., 2022).

Spectral measurements were performed on PAH mixtures, revealing a discrepancy of several nanometers between the extinction curve and the absorption peak of the PAH mixtures (Joblin et al., 1992).

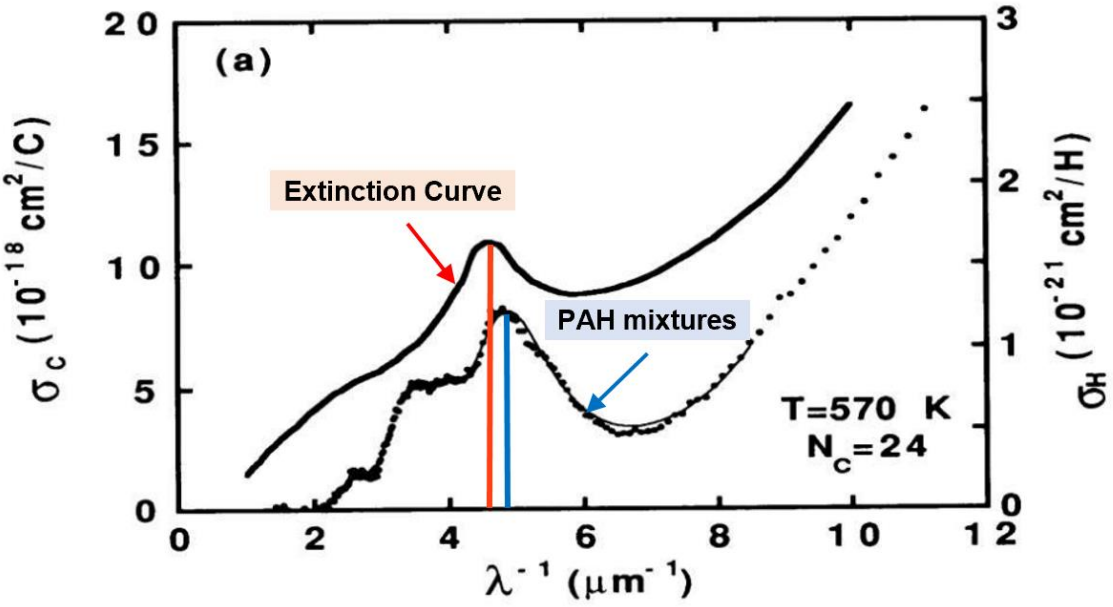

Figure 1.1.3 Extinction Curve compared with Absorption Cross Sections of PAH mixtures (Based on Joblin et al., 1992)

1.1.3 Space Weathering

Space weathering refers to the physical and chemical changes that occur on the surfaces of airless bodies or objects when exposed to interplanetary environments, resulting in alterations to their spectroscopic features. This process is primarily driven by micrometeoroid impacts, solar wind irradiation, and plasma interactions. Reddening or darkening of the surface is also a feature of space weathering.

Carbonization, a process involving the alteration of carbon-rich materials, is a significant aspect of space weathering. Papoular et al. (1996) observed a red shift in the reflectance spectra of coals in the UV region as the carbon content increased. In Figure 1.1.4, it can be observed that graphite, which has the highest carbon content among coals, exhibits an absorption peak shifted to the red compared to sub-bituminous coal, which has relatively lower carbon content.

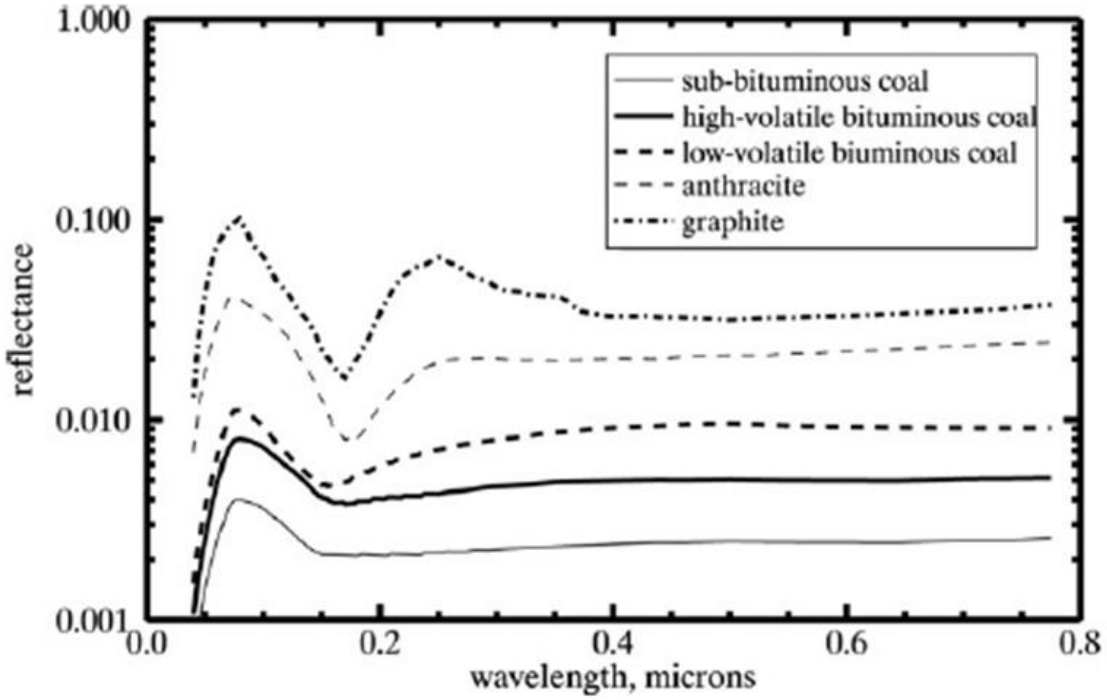

Figure 1.1.4 Coals with increasing carbon contents, showing that the absorption feature near 200 nm becomes stronger and narrower and shifted to the red (Based on Papoular et al. 1996 and Hendrix et al., 2016).

1.2. Research Objectives and Methodology

1.2.1 Research Objectives

Given that space weathering and carbonization can significantly impact the composition and spectroscopic properties of materials, studying the effects of space weathering on the spectra of polycyclic aromatic hydrocarbons (PAHs) is of paramount importance. Due to the proximity of the absorption peaks of PAHs to the UV bump at 217.5 nm in

the extinction curve, and considering that PAHs are organic compounds containing only carbon and hydrogen, serving as building blocks of life, studying the presence of PAHs in the interstellar medium is crucial for astrobiology and research on the origins of life.

1.2.2 Methodology

There are various approaches to studying space weathering, including the early analysis of Apollo samples and subsequent irradiation experiments conducted on the International Space Station. Among these methods, laboratory simulations of space weathering have become a widely used research technique.

To simulate space weathering, various methods have been developed (Moroz et al., 2014), such as plasma irradiation (Kimura et al., 2023), laser-based experiments (Sasaki et al., 2001), as well as low-energy H+ or He+ irradiation (Loeffler et al., 2009).

In this study, UV irradiation was used to simulate space weathering. In a vacuum environment, two different light sources were employed to irradiate PAH samples: a deuterium arc lamp and the 0th-order light from the synchrotron radiation source UVSOR. Two kind of PAH samples, coronene and anthracene, were used in this research. During the irradiation process, the vacuum system was connected to a Quadrupole Mass Spectrometer (QMS) to analyze substances that might be produced or undergo fragmentation during irradiation. Subsequently, we measured the UV spectra of both the unirradiated control group and the experimental groups exposed to different durations and light sources using the BL7B beamline at UVSOR, and analyzed any changes observed.

1.3. Thesis Structure

Chapter 1 provides the research background, including the significance of PAHs, the interstellar medium, and the extinction curve. It also discusses space weathering, outlines the research objectives and methodology, and presents the overall thesis structure.

Chapter 2 describes the preparation of PAH samples, detailing the thermal evaporation experiment and sample thickness measurement procedures, including data and results.

Chapter 3 outlines the purpose and procedure of the irradiation experiments, including the experimental setup, conditions, and light source flux estimation. It also covers the data result and analysis of the Quadrupole Mass Spectrometer.

Chapter 4 explains the setup and conditions for measuring absorption spectra, the data collection process, and presents the results and analysis for anthracene and coronene,

including error analysis.

Chapter 5 introduces the computational methods used, details the calculation procedures, and provides an analysis using Gaussian and PySCF tools, along with a comparative analysis.

Chapter 6 summarizes the main findings, discusses possible changes during space weathering, and suggests directions for future research.

2. Sample Preparation

2.1. Introduction

This study investigates the space weathering process of Polycyclic Aromatic Hydrocarbons (PAHs) and their impact on their spectral characteristics.

PAHs are organic molecules composed of multiple aromatic rings, found in various astronomical environments, including interstellar space and the atmospheres of planets. Among the numerous PAH molecules, coronene ($C_{24}H_{12}$) and anthracene ($C_{14}H_{10}$) were selected due to their structural characteristics and relevance to astronomical studies.

Coronene consists of seven fused benzene rings, forming a large, planar, hexagonal structure. It belongs to the broader class of PAHs and is known for its stability and occurrence in both terrestrial and extraterrestrial environments.

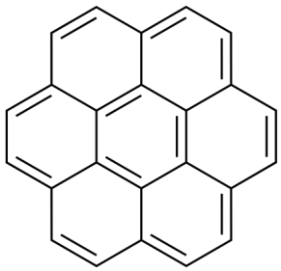

Figure 2.1.1 Coronene ($C_{24}H_{12}$)

Anthracene, composed of three fused benzene rings, is a planar, aromatic molecule that belongs to a larger family of carbon-based compounds. It is found both on Earth and in space, and its unique properties make it relevant to various astronomical studies.

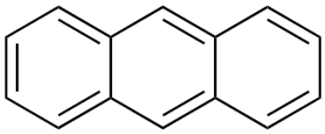

Figure 2.1.2 Anthracene ($C_{14}H_{10}$)

2.2. Thermal Evaporation Experiment

To fabricate samples suitable for measurement and as thin as possible, MgF_2 was used as substrates and employ the thermal evaporation method to condense the sample onto the substrate surface.

2.2.1. Sample Selection

For the experiments, commercially available coronene and anthracene were utilized. The coronene employed in experiments 2306, 2311, and 2406 was obtained from TCI, with varying levels of purity as follows:

- Experiment 2306: Coronene (purified by sublimation), CAS RN: 191-07-1, Product Code: C0386, with a purity greater than 95%.
- Experiments 2311 and 2406: Coronene (purified by sublimation), CAS RN: 191-07-1, Product Code: C1961, with a purity greater than 98%.

Anthracene used in these experiments was also sourced from TCI, characterized by the following specifications:

- Anthracene, CAS RN: 120-12-7, with a purity exceeding 90%.

Five to ten samples were prepared for each type of PAH to mitigate potential losses during sample preparation, transportation, and experimentation. This approach ensured sufficient material was available for all experimental phases.

For the substrate preparation, MgF_2 substrates manufactured by Japan Cell were employed. These substrates have a diameter of 10 mm and a thickness of 1 mm. Given the spectral properties of coronene and anthracene, the measurement range required spans from 170 nm to 400 nm. The 1 mm thick MgF_2 substrates maintain a transmittance of over 80% starting from 160 nm. Within the range of measurement needed, the transmittance remains consistently around 95%. This high and stable transmittance ensures that the transmitted light passing through the sample can effectively reach the photodiode, thereby maximizing measurement accuracy.

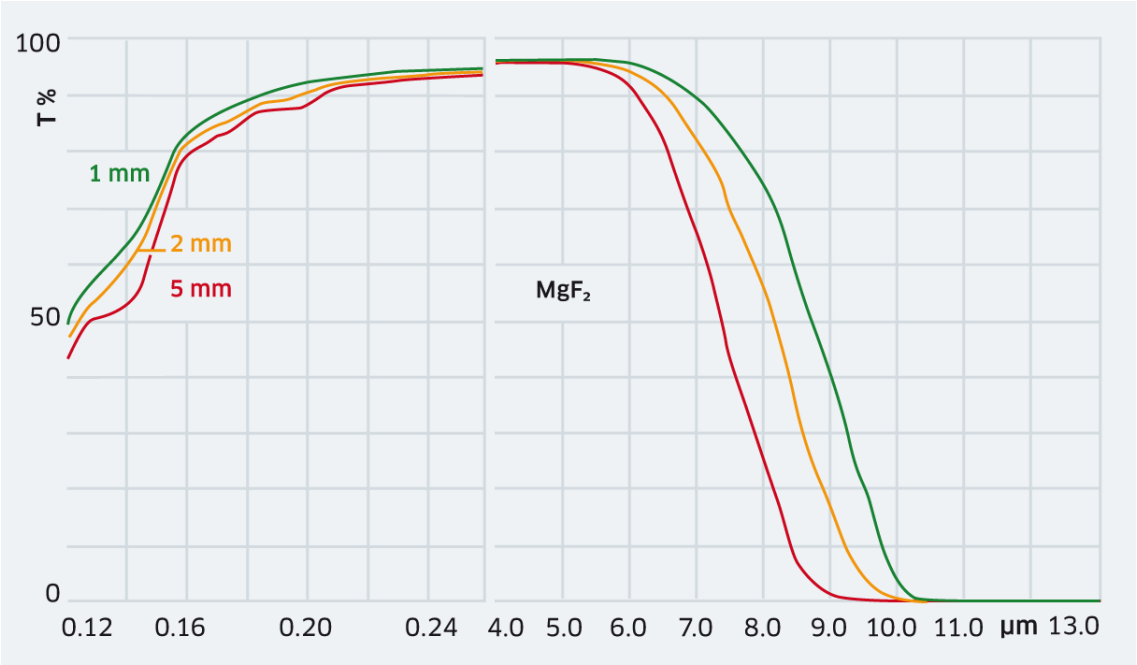

Figure 2.2.1 Commercially available MgF_2 transmittance curve (Source: LASEROPTIK GmbH Catalog 2023). X-axis represents the wavelength as µm, and Y-axis represents the transmittance ratio as percentage.

2.2.2. Experiment Procedure

The required amounts of coronene and anthracene powders were weighed. And the appropriate amount of sample powder was placed at the bottom of a vacuum tube. A support structure was positioned approximately ten centimeters above the powder, holding a 10 mm diameter, 1 mm thick MgF_2 substrate. The system was evacuated to a vacuum pressure maintained between 1 and 0.1 Torr.

The vacuum tube was inserted into the heating chamber's vertical opening, ensuring the substrate was near the outlet. For coronene, the optimal deposition was achieved by heating at 340 °C for four minutes. The heating process was carefully controlled to avoid the formation of coronene dimers, which can occur due to the breaking of C-H or C-C bonds at elevated temperatures, leading to the formation of more complex polymeric structures.

The tube was removed and allowed to cool to room temperature (approximately 25 °C). Atmospheric pressure was restored in the tube before extracting the sample. The sample thickness was initially assessed by visual inspection and color. The prepared samples were stored in a dry, light-protected environment, ready for subsequent experiments.

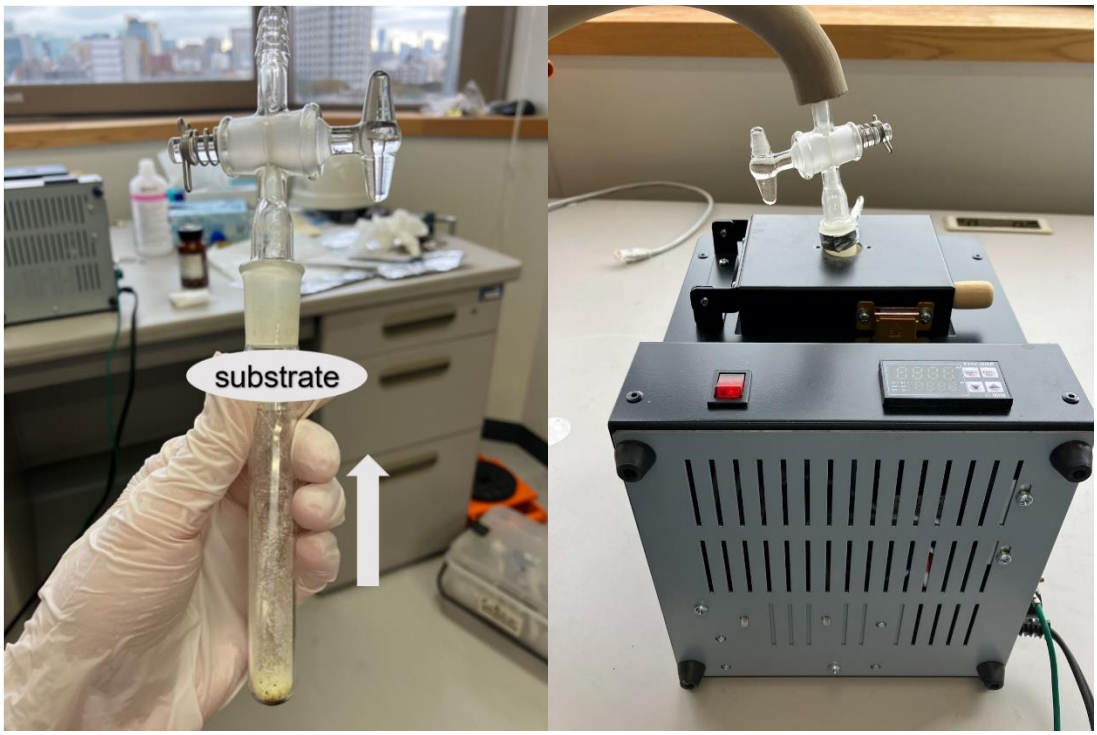

Figure 2.2.2 (Left) substrate placement and tube structure.
(Right) During the experiment, the tube was placed in the heating chamber.

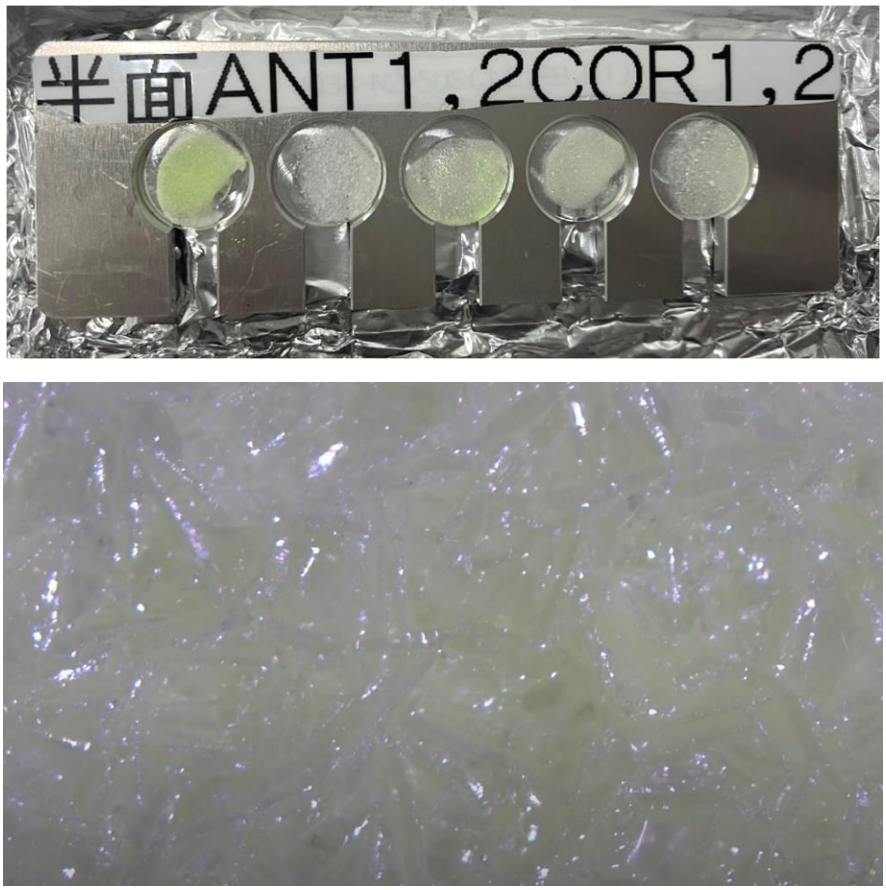

Figure 2.2.3 (Top) Anthracene samples used in the 2312 experiment. (Bottom) The anthracene sample surface under a microscope.

2.3. Sample Thickness Measurement

2.3.1. Measurement Procedure

Thickness measurements were conducted using the Mitaka NH Series "Laser Probe 3D Measuring Instrument" (Model: NH-3N), which has a measuring range of 150 x 150 x 10 mm (X, Y, Z) with an optional Z range of 110 mm and a scale resolution of 0.1 x 0.1 x 0.01 μm (X, Y, Z). The sample was placed on the measurement platform, and the laser was focused to ensure it passed through the sample's central axis. The computer system was then operated to select appropriate parameters and commence measurement, with the thickness data being accurately recorded.

Figure 2.2.4 3D Measuring Instrument.

Potential measurement discrepancies were observed when measuring the same reference plane before and after scanning uneven surfaces, likely due to a tilt in the measurement plane. To address this, the instrument was calibrated with a standard reference sample before and after each measurement, substrates with higher flatness were chosen to ensure uniform sample deposition, and samples were repositioned and re-measured if significant discrepancies were found.

2.3.2. Data and Results

In experiment 2406, all samples were coronene. Five samples were prepared, of which four were utilized. Thickness measurements indicated that all samples were approximately 100 microns thick.

In experiment 2312, two coronene samples were prepared, each with a similar thickness ranging from 150 to 200 microns. Additionally, in experiment 2312, most anthracene samples had a thickness between 100 and 200 microns. However, some thicker samples,

around 300 microns, were also produced but were not used in the experiments. Notably, post-irradiation, the samples tended to become thinner, typically measuring around 100 microns. Similarly, post-measurement, the samples also exhibited a reduction in thickness.

2.3.3. Conclusion

By carefully following these procedures, the accurate preparation and measurement of PAH samples were ensured, providing a solid foundation for subsequent UV irradiation and spectroscopic analysis.

3. Irradiation Experiment

3.1. Purpose

Following the preparation and measurement of PAH samples, UV irradiation experiments were carried out to simulate space weathering processes.

Space weathering to which objects are subjected in outer space includes UV irradiation. The study of the effects of space weathering on the structural and spectral properties of crown ethers and anthracenes by simulating space weathering through UV irradiation can increase the knowledge of the effects of space weathering on these organic compounds.

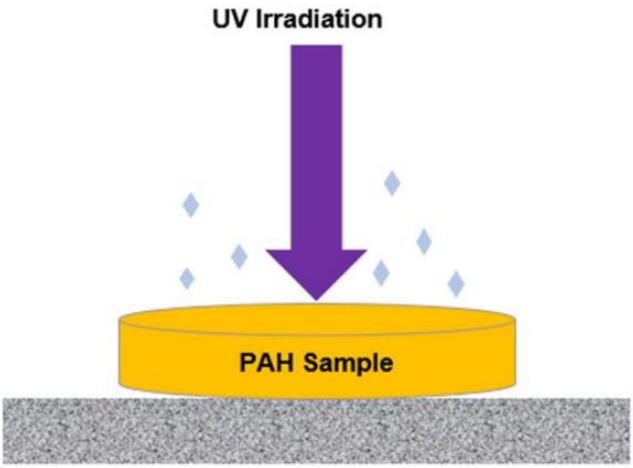

Figure 3.1 Irradiation Illustration.

3.2. Irradiation Experiment Procedure

3.2.1. Experimental Setup

In the experimental setup, sample fixation is achieved through a meticulously designed mounting system involving specific jigs. The front jig consists of an aluminum square plate featuring a central hole slightly smaller than the diameter of the sample. This configuration allows for maximal exposure of the sample surface, essential for uniform irradiation and consistent measurement results. The back jig, a larger aluminum plate, serves as a stable base and is directly affixed to the flange connection, ensuring a secure and precise alignment within the experimental apparatus.

In the course of the study, the experimental samples are encapsulated within a vacuum chamber, wherein the pressure is stringently regulated to approximately 10^{-5} Pa. Concurrently, the ambient temperature within the chamber is maintained at room temperature, approximately 20 °C to ensure thermodynamic stability and minimize thermal variations that could potentially affect the measurement outcomes.

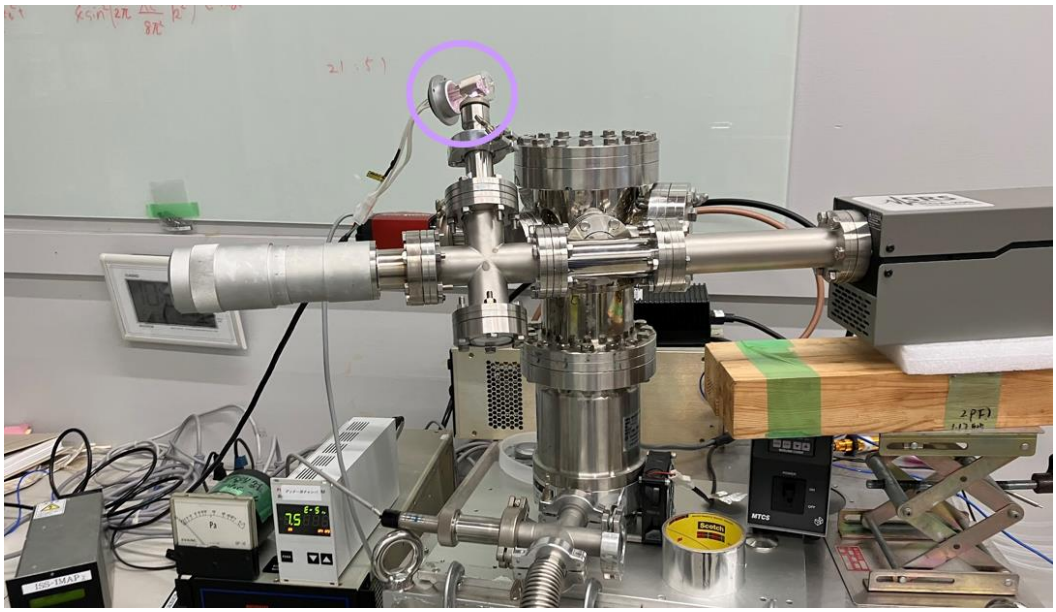

Figure 3.2.1 Experiment set up in the irradiation experiment using deuterium arc lamp.

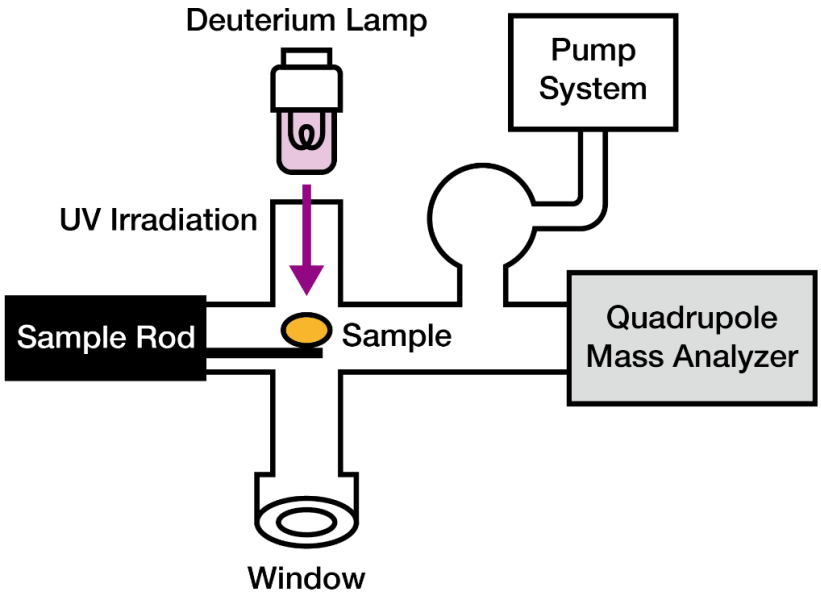

Figure 3.2.2 Illustration of experiment set up using deuterium arc lamp for irradiation.

Similar experiments were also conducted at UVSOR using 0^{th}-order light. Experiment Setup is similar as in Kashiwa Campus using the deuterium lamp.

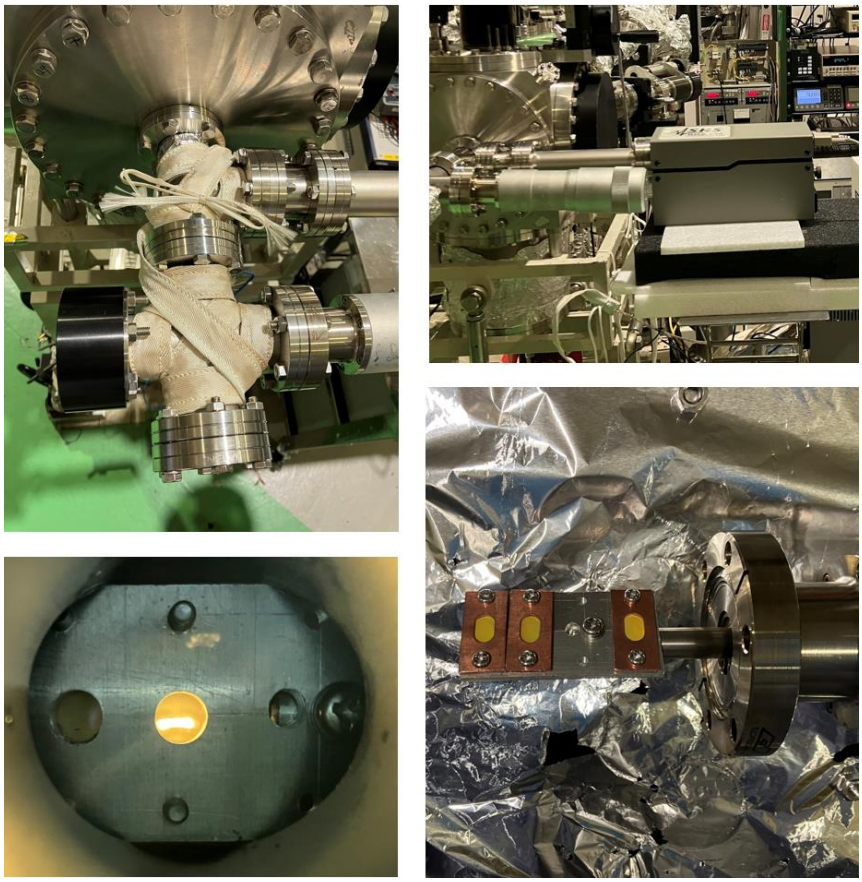

Figure 3.2.3 Irradiation experiment using 0^{th}-order light at UVSOR.
Top Left: Overview. Top Right: Quadrupole Mass Spectrometer.
Bottom Left: View from the back window for checking irradiation position on the sample. Bottom Right: sample rod with coronene samples on it.

3.2.2. Irradiation Conditions

The exposure durations for the UV irradiation experiments were systematically varied according to the type of PAH and the UV light source employed.

For coronene, irradiation was performed using a deuterium lamp for 3 hours, 6 hours, and 12 hours, and using the UVSOR synchrotron source for 3 hours, 6 hours, and 8 hours. In the case of anthracene, exposure durations were 1 hour, 1.5 hours, and 3 hours with the deuterium lamp, and 1 hour, 3 hours, and 6 hours with the UVSOR source.

It is noteworthy that complete evaporation of anthracene was observed after 6 hours of exposure to the UVSOR source, likely due to photodissociation.

Figure 3.2.3 Anthracene samples before (Top) and after (Bottom) irradiation of deuterium arc lamp.
(Left to Right: anthracene with no irradiation, 3 hours irradiation, 1.5 hours irradiation, 6 hours irradiation, 6 hours irradiation.)

After 6 hours of irradiation, the anthracene samples become predominantly transparent, with only the MgF_2 substrate remaining. Additionally, samples subjected to 3 hours and 1.5 hours of irradiation exhibit reduced thickness and a noticeable whitening effect.

3.2.3. Light Source Flux Estimation

3.2.3.1 Deuterium Arc Lamp

In this experiment, the sample was irradiated with ultraviolet light emitted from a deuterium lamp (Hamamatsu Photonics L9841). This light source utilizes arc discharge in deuterium gas to emit light and is characterized by a stable light output drift of approximately ±0.3%. The flux and light distribution characteristics are described in the Hamamatsu Photonics catalog.

In Figure 3.2.4, the emission spectrum distribution for three types of window materials is shown, the lamp used in this experiment had magnesium fluoride (MgF_2) as the window material. In general, the transmittance of glass materials in the far-ultraviolet region is low, but MgF2 shows a transmittance of over 50% even at a short wavelength of 120 nm.

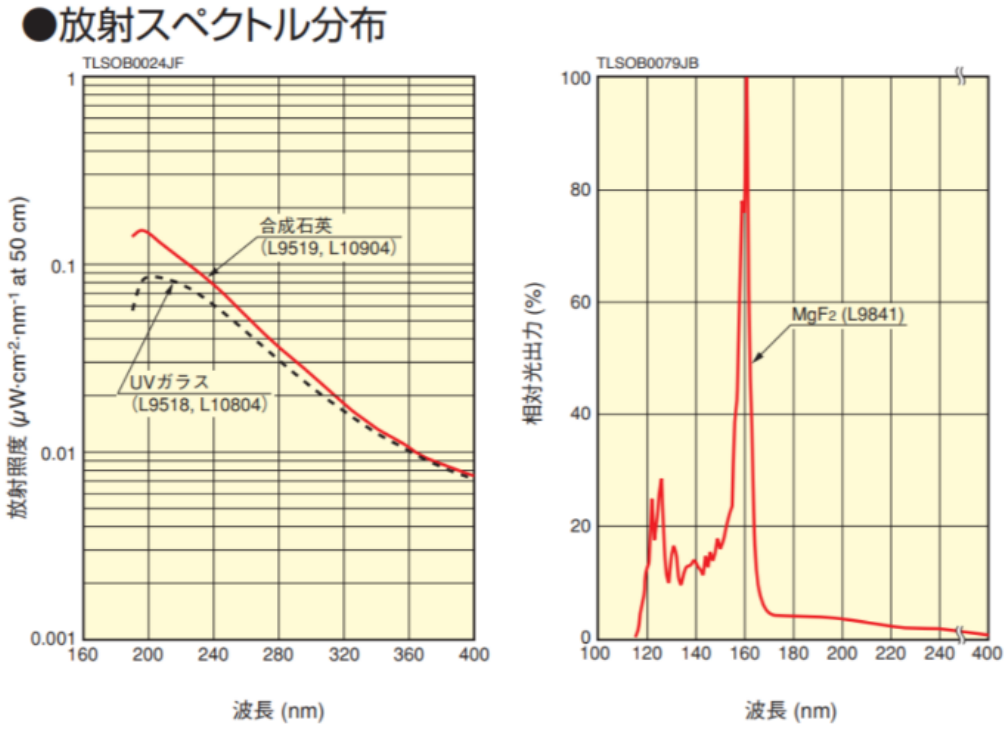

Figure 3.2.4 The emission spectra of the deuterium arc lamp.
(Source: Hamamatsu Photonics catalog:
https://www.hamamatsu.com/resources/pdf/etd/D2lamps_TLS1017J.pdf)

The relationship between light intensity and distance is described by the inverse square law, a fundamental principle in photometry and radiometry. This law states that the

intensity of light emanating from a point source is inversely proportional to the square of the distance from the source. Mathematically, it is expressed as:

$$I \propto \frac{1}{d^2}$$

As the light intensity at a distance of 50 cm (I_{50}) is known, the intensity at a distance of 20 cm (I_{20}), apply the inverse square law as follows:

$$\frac{I_{20}}{I_{50}} = \left(\frac{d_{50}}{d_{20}}\right)^2 = \left(\frac{50}{20}\right)^2 = 6.25$$

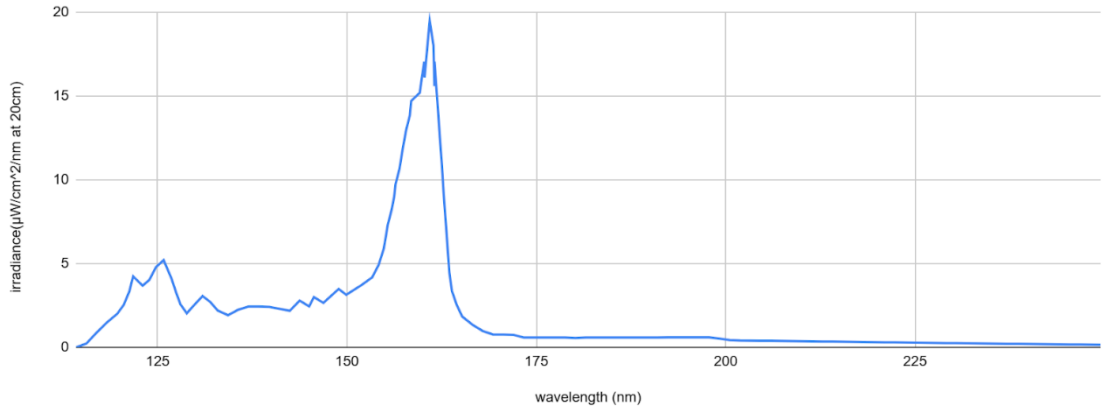

Figure 3.2.5 Radiation Intensity Distribution of the Lamp with a distance of 20 cm with MgF_2 as the Window Material

Next, the light distribution characteristics are considered. According to the catalog, the deuterium lamp exhibits angular dependence in its light distribution characteristics, as shown in Figure 3-6. However, for simplicity, we assume that the irradiance is uniform within ±5° in all directions for the purpose of evaluating the light intensity.

In this experiment, ultraviolet irradiation on the polystyrene sample was conducted at a distance of approximately 20 cm from the lamp's emission point. Given that the diameter of the irradiated area (approximately 1 mm) is smaller than 20 cm × tan 5° ≅ 17 mm, we assume that the irradiated light intensity was uniform.

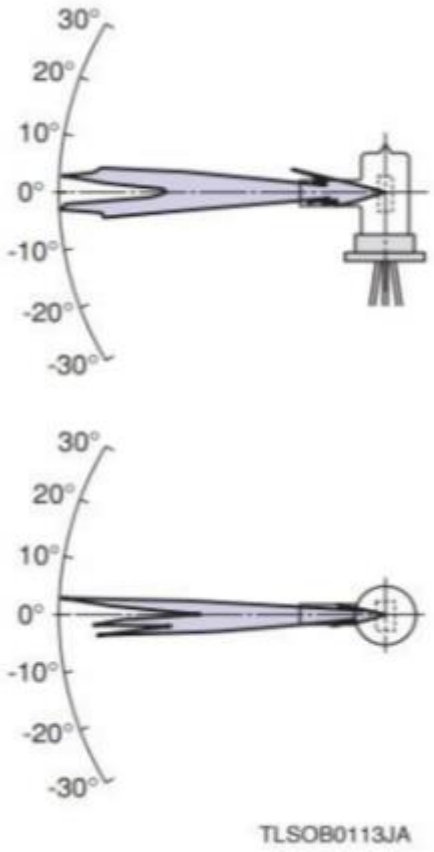

Figure 3.2.6 Light distribution characteristics of the Deuterium Lamp
(Source: Hamamatsu Photonics catalog)

Therefore, the intensity distribution can be calculated. As it can be seen from the figure, the intensity of deuterium lamp irradiation in the far UV region is 10 to 10^3 times of the solar irradiation intensity (Gueymard 2004). After 200 nm, the intensity of deuterium lamp is $\frac{1}{10}$ to $\frac{1}{10^3}$ of the solar irradiance.

Under this estimation, 1 hour of irradiation under deuterium lamp equals to 42 days irradiance at 1 AU by the sun. 3 hours of irradiation under deuterium lamp equals to 123 days irradiance at 1 AU by the sun. And 12 hours of irradiation equals to 1.37 years of irradiation at 1 AU by the sun.

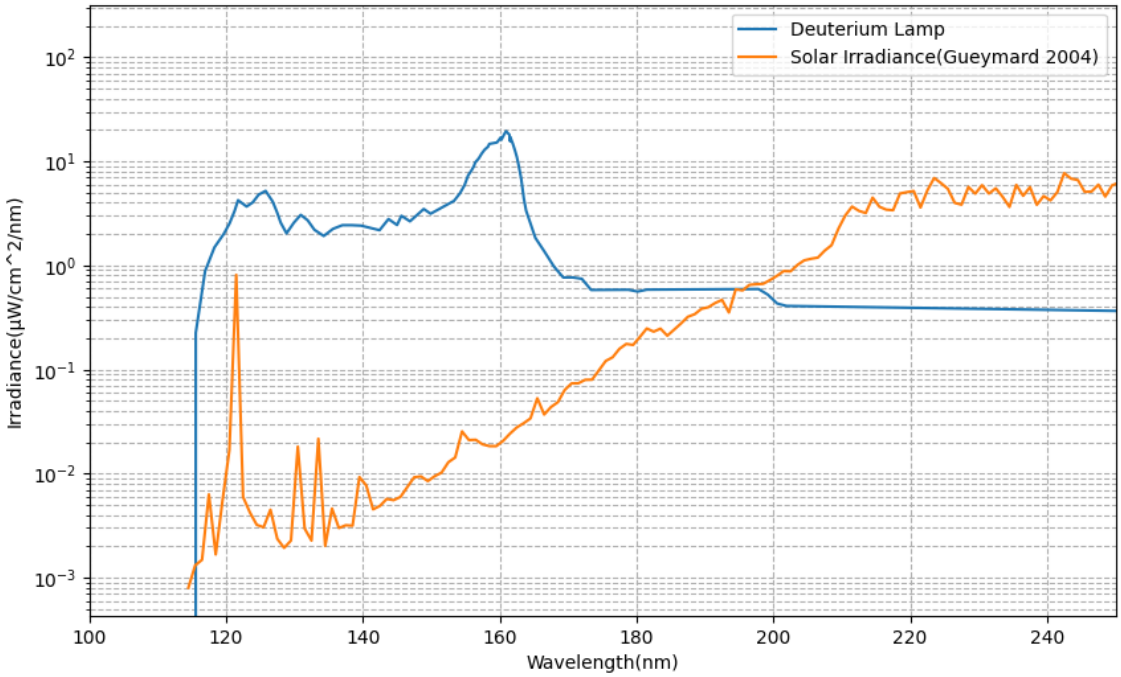

Figure 3.2.7.a The comparison of intensity between deuterium lamp irradiation and solar irradiance from 100 nm to 240 nm.

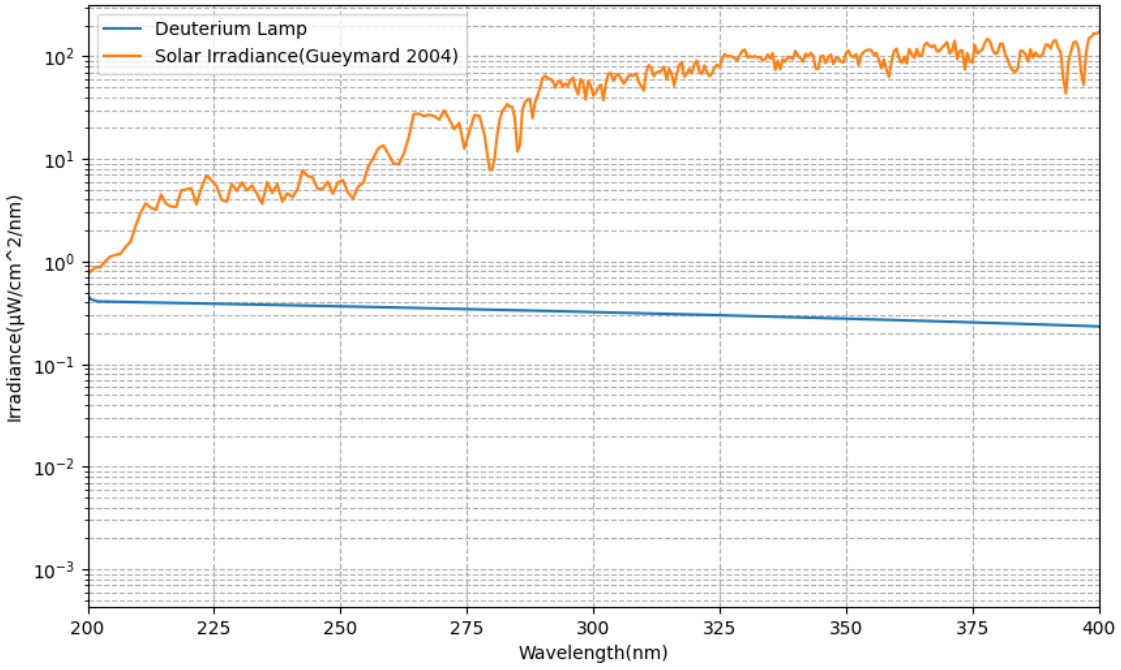

Figure 3.2.7.b The comparison of intensity between deuterium lamp irradiation and solar irradiance from 100 nm to 240 nm.

3.2.3.2 0th-Order Light at UVSOR

To simulate space weathering, powerful zero-order light emitted from the synchrotron facility UVSOR was used for irradiation. As the photodiode used for spectral measurements is unable to directly measure the intensity of light, the irradiation intensity can be indirectly estimated from various parameters.

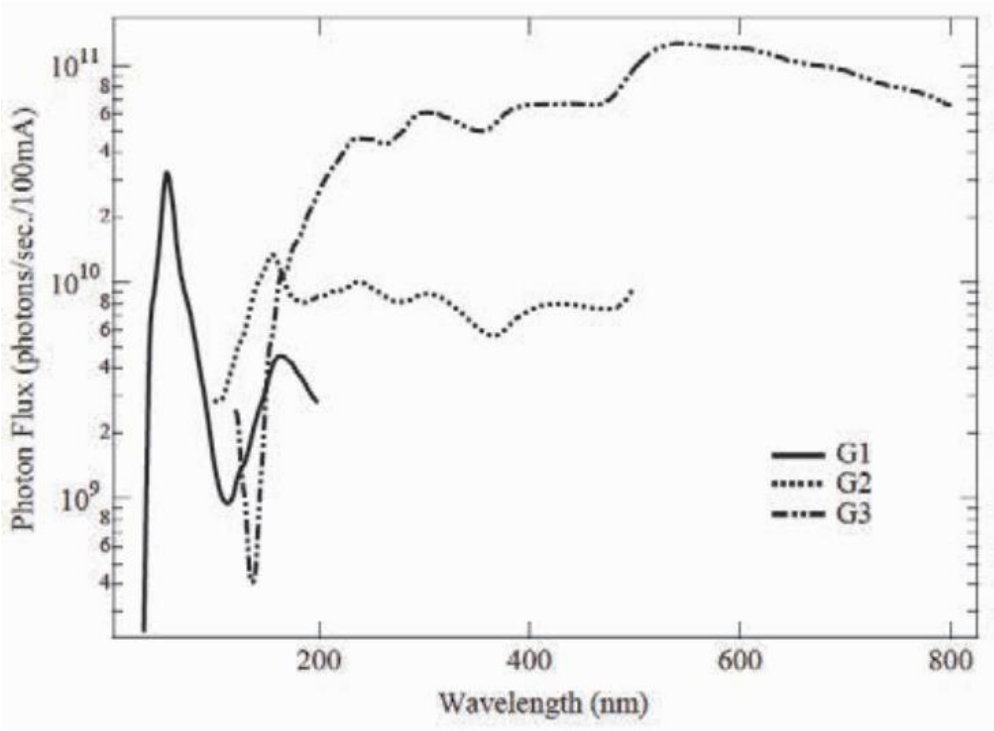

Figure 3.2.8 Throughput spectra of the beamline BL7B at UVSOR measured using a silicon photodiode. (Source: UVSOR Activity Report 2024)

According to official documentation from UVSOR, the energy resolution ΔE/E ranges from 4000 to 8000. The 0th-order light output typically uses the G2 grating, which yields a photon flux of approximately $10^{10}\ photons/sec/100mA$. Since 2023, the beam current at UVSOR has been maintained at around 200 mA. Generally, light intensity decreases to 1/10 after reflection.

Based on a rough estimation, it is reasonable to assume that the energy resolution is approximately 5000. Given the Planck formula,

$$E\ = hv = \frac{hc}{\lambda}$$

where h is the Planck constant and c is the speed of light, the wavelength resolution can be derived from the energy resolution:

$$\frac{\Delta\lambda}{\lambda} = \frac{1}{5000}$$

For λ = 200 nm, $\Delta\lambda = 4 \times 10^{-2}\ nm$.

Considering the photon flux is around 10^{10} photons/sec/100mA and the beam current is about 200 mA, if the photon flux is assumed to be uniformly distributed from 200 nm to 700 nm, the photon flux can be calculated as follows:

$$\left(\frac{10^{10}}{4 \times 10^{-2}}\right) \times 500 \times 2 \times 10\ photons/sec/mm^2 \approx 10^{17}\ photons/sec/cm^2$$

For a rough comparison, the photon flux at 1216 Å (Lyα) of the sun at 1 AU is approximately $3.9 \times 10^{11} \pm 0.15 \times 10^{11}$ photons/sec/cm^2(White et al., 1990). Therefore, the solar flux can be assumed to be around 10^{12} photons/sec/cm^2.

Under this estimation, 1 hour of irradiation by the 0th-order light at UVSOR approximately equals 11 years of solar irradiation at 1 AU. Similarly, 3 hours of irradiation at UVSOR equals about 34 years, and 8 hours of irradiation equals approximately 91 years of solar exposure at 1 AU.

3.3. Quadrupole Mass Spectrometer

3.3.1. Data and Results

Continuous monitoring during the irradiation process was conducted using a Quadrupole Mass Spectrometer (QMS). The QMS consists of four parallel cylindrical rods that perform mass analysis based on the mass-to-charge ratio (m/z) of ions. Ion separation in the QMS is achieved by maintaining stable ion trajectories within oscillating electric fields. This setup allows for precise tracking of ion behavior throughout the irradiation process, providing valuable data for the analysis of molecular changes and the identification of photoproducts formed during UV exposure.

In the six-hour irradiation experiment of anthracene, it was found that after six hours of deuterium arc lamp irradiation, the sample completely disappeared, leaving only the substrate itself. Initially, sample peeling was considered, but after repeated experiments and examination of the QMS scan data, it was confirmed that this is due to the evaporation and photodecomposition of anthracene under UV irradiation. Previous research also suggests the destruction and ionization of PAHs (Monfredini et al., 2019).

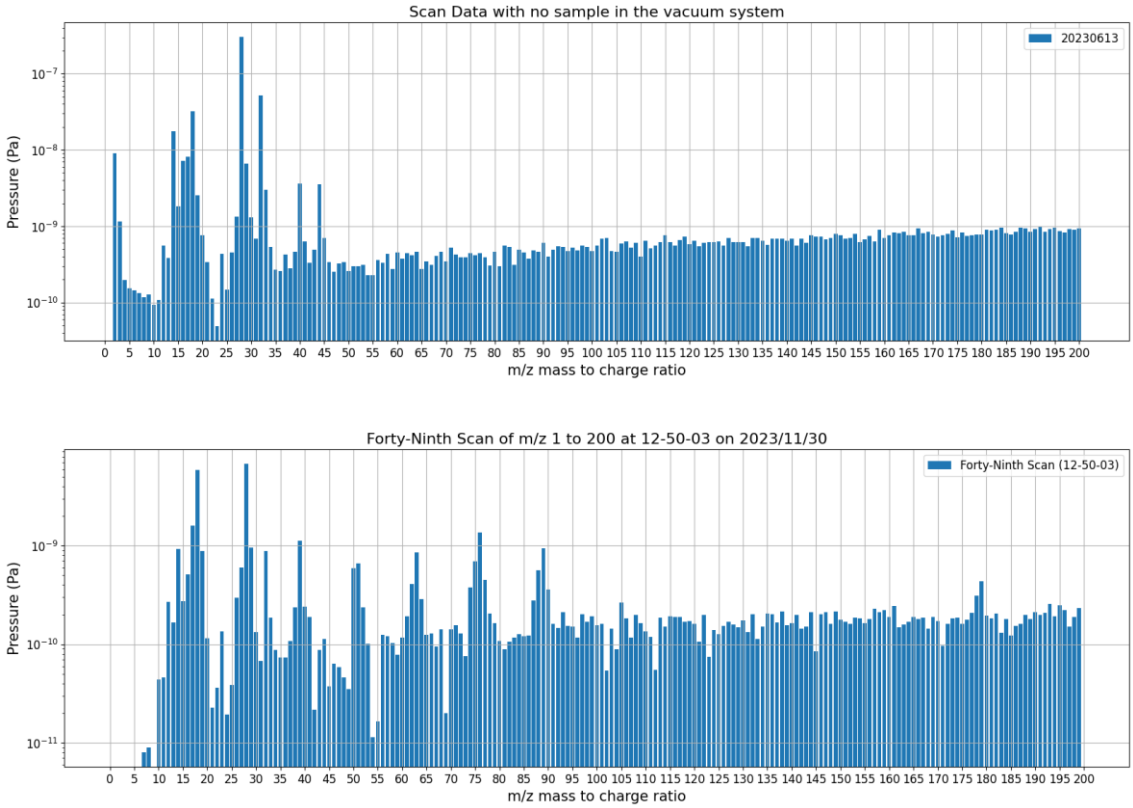

Figure 3.3.1 Scan (Top) with no irradiation and after (Bottom) one-hour irradiation.

By comparing the scans before irradiation and one hour after the start of irradiation, it was found that in addition to common gases that exist in the atmosphere and vacuum systems such as $H_2O(18)$ and $N_2(28)$, these peaks remained. New peaks, such as 39, 50, 63, 76, and 89, were also observed, and adjacent values increased as secondary peaks. Notably, a small peak appeared at 178.

Additionally, the time variation of each m/z with significant changes was calculated. By computing the overall mean variation over time and the variance of each m/z from the mean variation line, it was identified which m/z had the largest changes during irradiation. The top 20 m/z values with the largest changes were extracted and analyzed.
1, 28, 18, 76, 2, 39, 89, 63, 17, 3, 51, 88, 178, 75, 50, 32, 27, 19, 14, 77
These are the m/z values with the largest changes.

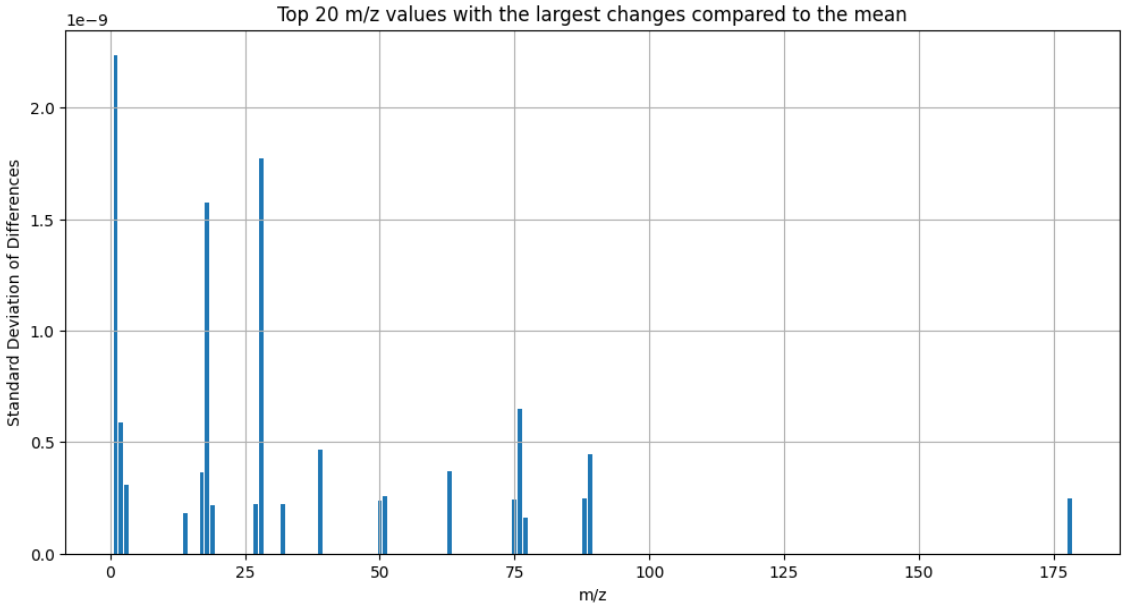

Figure 3.3.2 Top m/z values with the largest changes compared to the mean value of time variation pressure

3.3.2 Analysis

By comparing the common gas library and possible fragmentation products of anthracene's C and H ions or molecules, the following can be concluded:

m/z 39:

Ar(Argon): One of the isotopes of argon, Ar-39, has an m/z of 39.

$C_3H_3^+$(Cyclopropyl or allyl ion): A common organic molecule fragment composed of three carbon atoms (total m/z of 36) and three hydrogen atoms (total m/z of 3), making a total m/z of 39.

K^+(Potassium ion): One of the isotopes of potassium, K-39, is a common source of m/z 39.

m/z 63:

CH_3Cl(Chloromethane): Composed of one carbon atom (m/z 12), three hydrogen atoms (total m/z 3), and one chlorine atom (m/z 35), total m/z of 50, but its isotopic peak may appear around 63.

Cu(Copper isotope): One of the isotopes of copper is Cu-63, with an m/z of 63.

$C_5H_3^+$: An organic molecule fragment composed of five carbon atoms (total m/z 60) and three hydrogen atoms (total m/z 3), a total m/z of 63.

m/z 76:

SO_2(Sulfur dioxide): Composed of one sulfur atom (m/z 32) and two oxygen atoms (each m/z 16), total m/z of 76. Sulfur dioxide may be present in the air.

$C_6H_4^+$: Composed of six carbon atoms (total m/z 72) and four hydrogen atoms (total m/z 4), making a total m/z of 76. This fragment may come from the breakdown of larger polycyclic aromatic hydrocarbons.

m/z 89:

$C_3H_7NO_2$(Alanine): A common amino acid with an m/z of 89, but in mass spectrometry, an m/z of 89 is more likely a fragment.

$C_7H_5^+$: An organic molecule fragment composed of seven carbon atoms (total m/z 84) and five hydrogen atoms (total m/z 5), making a total m/z of 89.

$C_4H_9O^+$: For example, tert-butoxy ion.

In the photodissociation of $C_{14}H_{10}$ (anthracene), possible fragments include:

m/z 39: Possibly $C_3H_3^+$, from the decomposition of polycyclic aromatic hydrocarbons.

m/z 63: Possibly $C_5H_3^+$, from the decomposition of larger carbon-hydrogen molecules.

m/z 76: Possibly $C_6H_4^+$, from the decomposition of larger carbon-hydrogen molecules.
m/z 89: Possibly $C_7H_5^+$, or other larger organic molecule decomposition products.

By analyzing the time variation of these m/z values, we extracted 18, 28, 39, 76, and 178 as examples. It was found that 18 and 28 showed significant changes.

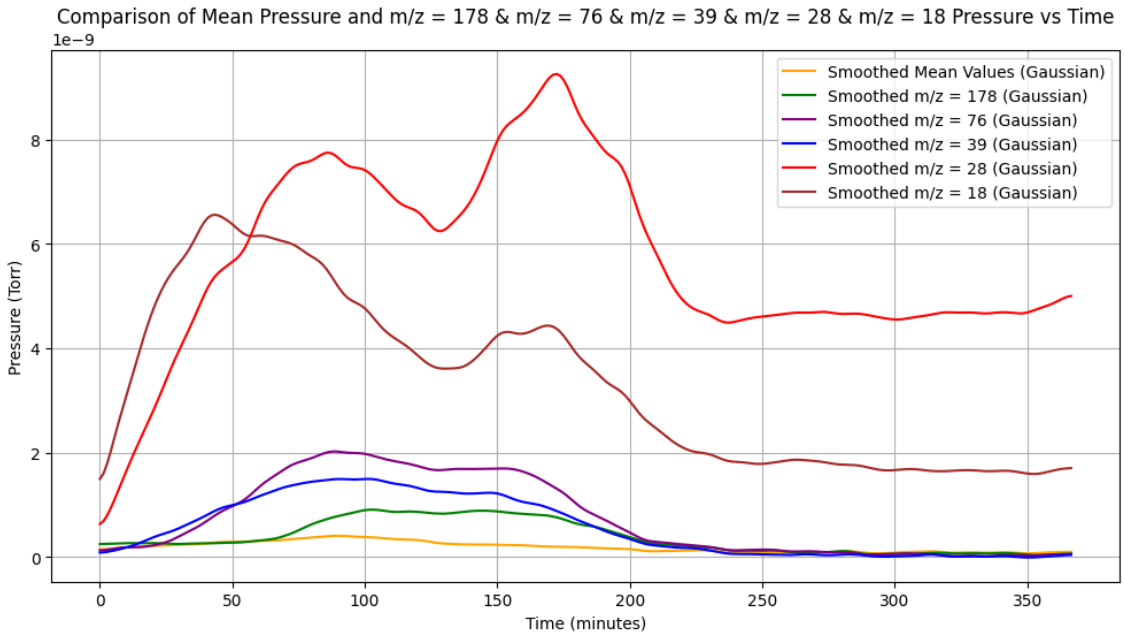

Figure 3.3.3 Comparison of mean pressure and m/z = 178 & m/z = 76 & m/z = 39 & m/z = 28 & m/z = 18 Pressure vs Time

Further analysis of m/z 178, 76, and 39 revealed substantial deviations from the mean. It can be observed that smaller m/z values started to increase earlier, almost immediately after irradiation started, while m/z 178 increased later, around one hour after irradiation began.

It can be inferred that smaller molecules escape from the surface more readily under short-time irradiation, likely due to the lower energy required for bond dissociation. After an hour of irradiation, anthracene as a whole molecule also undergoes photo vaporization.

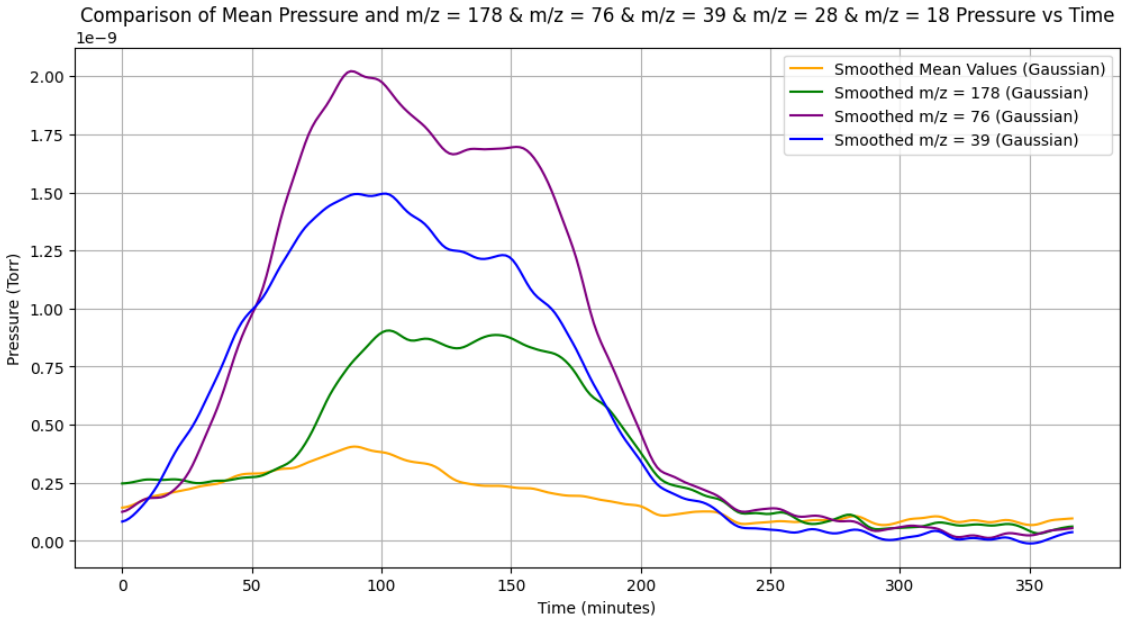

Figure 3.3.4 Comparison of mean pressure and m/z = 178 & m/z = 76 & m/z = 39 Pressure vs Time

Of particular note, the m/z=1 values were negative, which is unrealistic and therefore not reported.

4. Absorption Spectra Measurement

4.1. Introduction

Due to the limitations in sample thickness, the transmittance light signal is relatively weak, necessitating the use of a stronger intensity UV light source to obtain accurate measurements.

The spectra measurements were conducted at UVSOR, a synchrotron radiation facility within the Institute for Molecular Science, part of the National Institutes of Natural Sciences. One of the UVSOR beamlines, the BL7B beamline was utilized for these experiments.

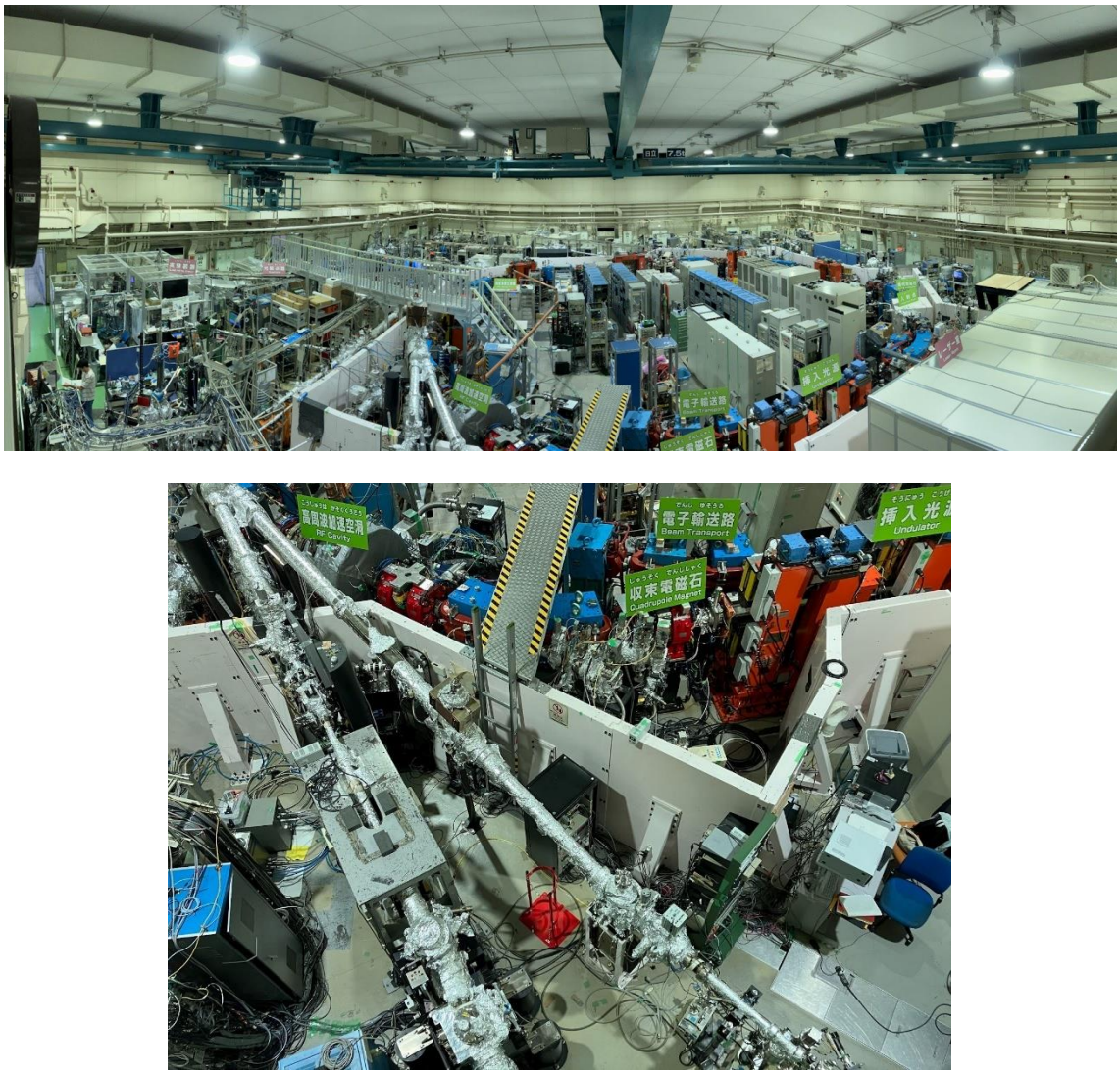

Figure 4.1.1 (Top) UVSOR overview and (Bottom) beamline BL7B

The BL7B beamline specifications include an energy range of 1.2 eV to 25 eV, a wavelength range of 50-1000 nm, and a resolution characterized by $E/\Delta E=4000-8000$ with 0.01 mm slits. It supports various spectroscopic experiments, including absorption, reflection, and fluorescence spectroscopy, primarily for solid-state samples.

Additionally, LiF, MgF_2, Pyrex, and Quartex window valves are installed between the beamline end valve and the focusing position, providing flexibility for various experimental configurations.

4.2. Experiment Setup and Conditions

4.2.1 Experiment Setup

The sample needs to be installed in the vacuum chamber before measurement. There is a flange at the top of the vacuum chamber that can hold a rod. The part extending into the vacuum chamber can be used to secure the sample plate with screws. The part outside the vacuum chamber can control the movement of the sample plate inside the vacuum chamber along the XYZ axes.

After placing the sample, the photodiode should be connected to the amplifier box and fixed on the base in the vacuum chamber, which can move around the sample rod. A small piece of highly reflective Si plate should be attached to the window of the photodiode box, and the position corresponding to the photodiode should be marked on the Si plate. Then, turn on the zero-order light to ensure that the sample can be smoothly irradiated and that the transmitted light can reach the central area of the photodiode's surface.

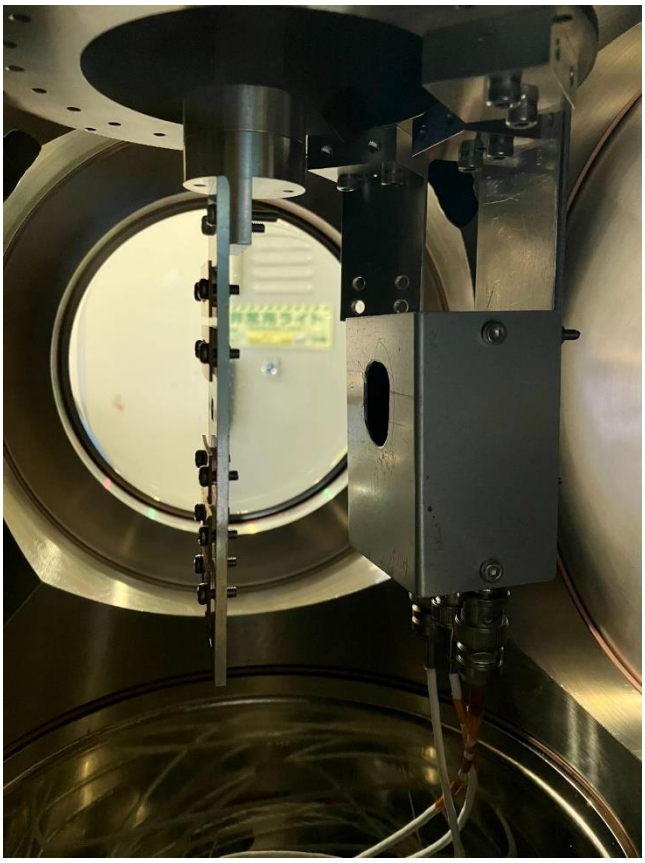

Figure 4.2.1 Experiment Setup (Left: Samples on the rod. Right: Photodiode in the amplifier case)

4.2.2 Photodiode and Pre-Amplifier

During spectra measurement, AXUV100HYBI is used as the amplifier, and AXUV100 is used as the photodiode. The AXUV100HYBI is a high vacuum-compatible current-to-voltage converting amplifier specifically designed for use with AXUV100 and AXUV20 photodiodes. It can measure small photogenerated currents with resolutions of 10 femtoamperes and has a dynamic range spanning four orders of magnitude. The amplifier consists of a very low noise operational amplifier with a 100 GΩ high feedback resistor, and all components have low tolerances to ensure consistent current-to-voltage transfer characteristics with minimal offset voltage.

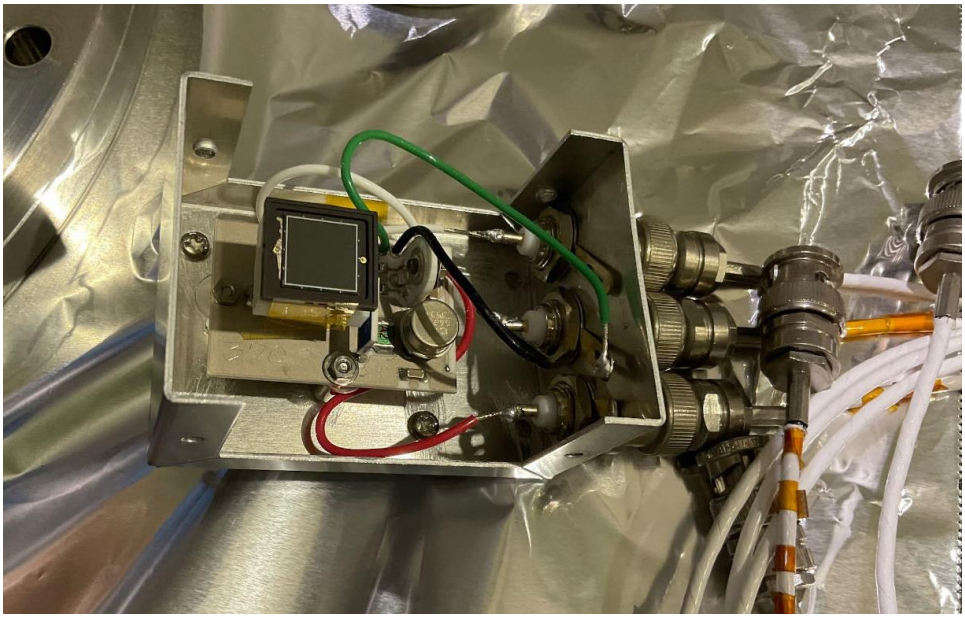

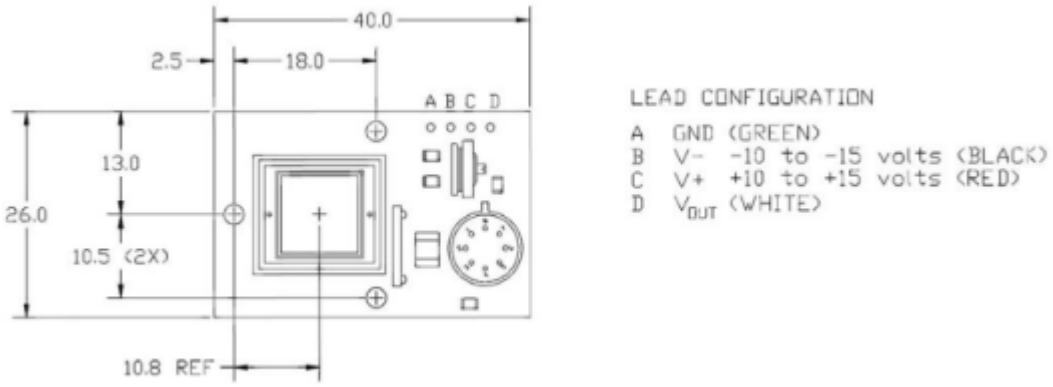

Figure 4.2.2 (Top) Photodiode on the amplifier AXUV100HYBI
(Bottom) AXUV100HYBI configuration (Source: IRD Catalogue, 2007).

In the experiment, the amplifier circuit was repaired and replicated on a breadboard, and an amplified signal consistent with the official specifications was obtained.

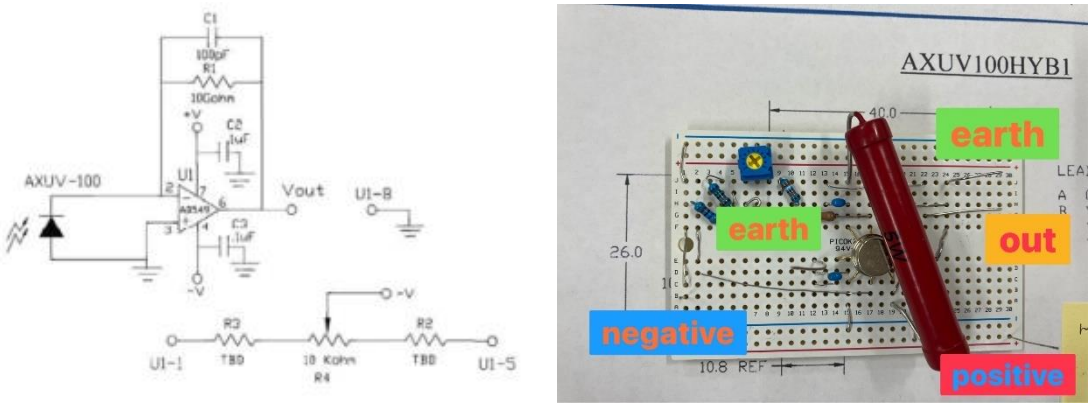

Figure 4.2.3 (Top) Circuit layout (Source: IRD Catalogue, 2007).
(Bottom) Replicated circuit on a breadboard.

Testing confirmed that the input and output signals are consistent with the basic analog signals, as is shown in Figure 4.2.4.a and Figure 4.2.4.b.

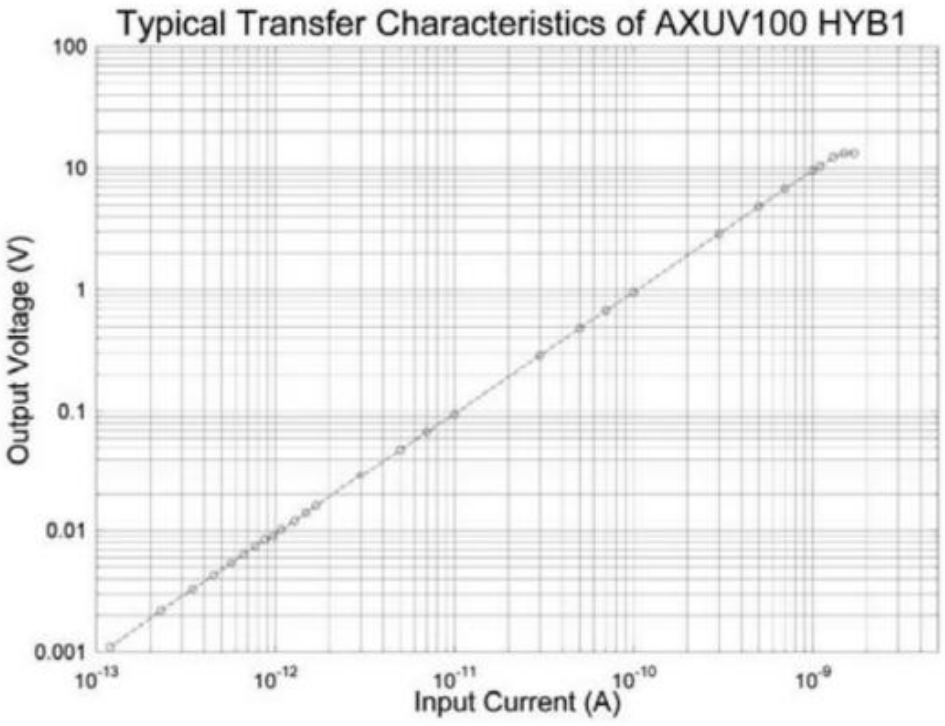

Figure 4.2.4.a AXUVHYBI transfer characteristics (Source: IRD Catalogue, 2007).

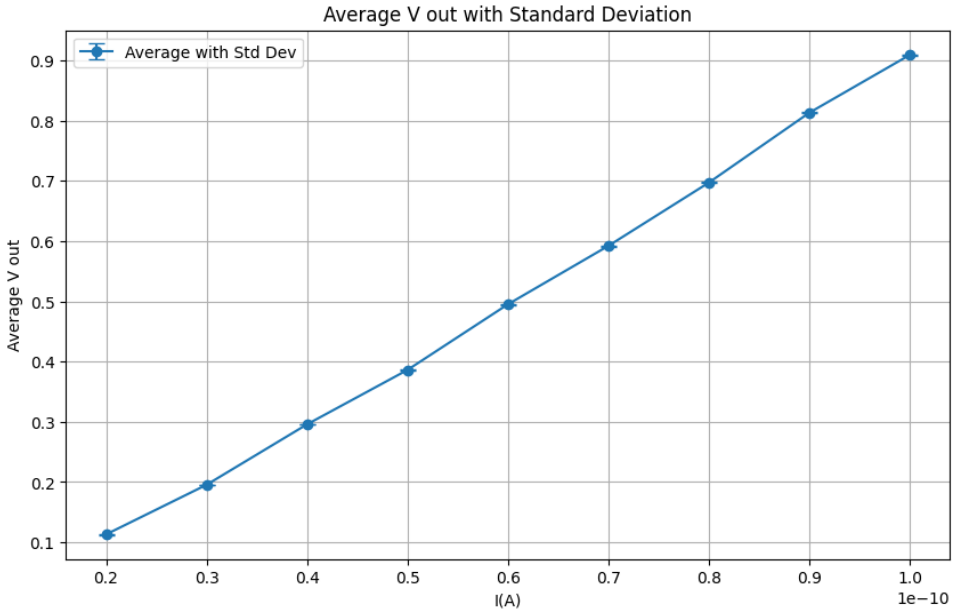

Figure 4.2.4.b The experiment data obtained from the breadboard.

4.2.3 Measurement Conditions

To initiate the alignment process, the 0th-order light source is activated, ensuring proper illumination of the sample for accurate measurements. It is crucial to verify that the transmitted light precisely targets the central area of the photodiode surface, ensuring optimal detection and data accuracy.

Experiments were conducted under controlled environmental conditions, with the temperature maintained at approximately 20 °C and the vacuum chamber pressure at around 10^{-5} Pa. These conditions are essential for minimizing external influences and ensuring the reliability of the experimental results.

4.3 Data Collection

4.3.1 Measurement Principles

The transmitted light passes through the sample and reaches the surface of the photodiode, which subsequently converts the optical signal into an electrical signal. This electrical signal is then amplified by a preamplifier and converted into a digital signal by the electrometer. The digitized data is collected and analyzed by the computer.

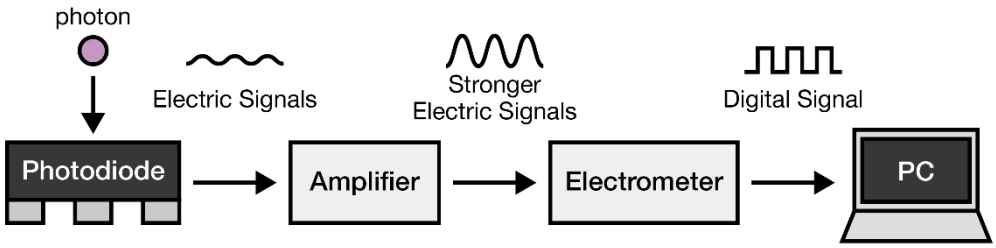

Figure 4.3.1 Flowchart of Optical Signal Conversion to Digital Signal

4.3.2 Data Structure

4.3.2.1 Data Set

During each measurement session, multiple types of data are collected. These include:

- **Dark Noise (dark)**: Background data of dark noise is measured.
- **Direct (direct)**: Data of light directly reaching the surface of the photodiode is measured.
- **Transmission (trans)**: Data of transmitted light passing through the sample and hitting the photodiode is measured.

Each set of measurements typically comprises 15 measurements: eight measurements of dark noise (dark_1, dark_2, dark_3, dark_4, dark_5, dark_6, dark_7, dark_8), four measurements of direct light (direct_1, direct_2, direct_3, direct_4), and three measurements of transmitted light (trans_1, trans_2, trans_3). Each data point represents the digital signal converted from the light intensity received per nanometer.

4.3.2.2 Data Segment

To avoid the influence of higher-order light, the spectral measurement is segmented. Different filters were used at different ranges.

- Coronene： The measurement range is 170 nm to 370 nm, divided into two parts for measurement.
  170 nm to 300 nm
  300 nm to 370 nm
- Anthracene： The measurement range is 200 nm to 400 nm, divided into two parts for measurement.
  200 nm to 300 nm
  300 nm to 400 nm

4.3.2.3 Higher-Order Light

In UV measurements, using a filter to reduce higher-order light (light at multiples of the fundamental wavelength) is crucial. Diffraction gratings disperse polychromatic light into its constituent wavelengths, but higher-order diffraction can produce unwanted light at multiples of the desired wavelength. This higher-order light can interfere with measurements, causing inaccuracies. Filters effectively block these higher-order wavelengths, ensuring only the desired light reaches the detector. This enhances measurement accuracy by eliminating noise and potential spectral overlap, providing a clearer and more precise spectral analysis.

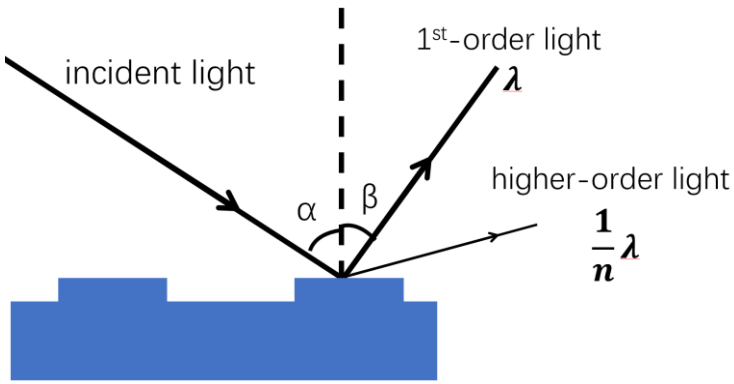

Figure 4.3.2 Laminar-Type Grating, incident light, 1st-order light and higher-order light

For the measurement from 170 nm to 300 nm and 200 nm to 300 nm, Quartz is used as the filter as it has a cutoff wavelength of around 155 nm, and therefore can greatly reduce the higher-order light shorter than 310 nm.
Similarly, the Pyrex filter which has a cutoff wavelength of around 250 nm was used for measurement from 300 nm to 400 nm, and therefore can greatly reduce the higher-order light shorter than 500 nm.

4.3.2 Data Calculation

4.3.2.1 Calculating of Transmittance Ratio

For each direct measurement, the average of the preceding and following dark measurements was subtracted to obtain the direct-dark values. Similarly, for each trans measurement, the average of the preceding and following dark measurements was subtracted to obtain the trans-dark values. The calculations are as follows:

For direct_1:

$$dark_{1,2} = \frac{dark_1 + dark_2}{2} \quad (4-1)$$

$$direct\_dark_1 = direct_1 - dark_{1,2} \quad (4-2)$$

Similar calculations were conducted for direct_2, direct_3, and direct_4.

For trans_1:

$$dark_{3,4} = \frac{dark_3 + dark_4}{2} \quad (4-3)$$

$$direct\_dark_1 = direct_1 - dark_{3,4} \quad (4-4)$$

Similar calculations were conducted for trans_2 and trans_3.

To obtain a representative value for the direct-dark and trans-dark measurements, the averages of the respective sets were calculated:

$$direct\_average\_dark = \frac{direct\_dark_1 + direct\_dark_2 + direct\_dark_3 + direct\_dark_4}{4} \quad (4-5)$$

$$trans\_average\_dark = \frac{trans\_dark_1 + trans\_dark_2 + trans\_dark_3}{3} \quad (4-6)$$

The transmission ratio T was calculated as:

$$T = \frac{trans\_average\_dark}{direct\_average\_dark} \quad (4-7)$$

4.3.3.3 Calculation of Absorption Ratio

Usually, absorption ratio can be calculated as,

$$absorption\ ratio = 1 - transmittance\ ratio - reflectance\ ratio \qquad (4-8)$$

However, for thin layers,

$$reflectance\ ratio \ll transmittance\ ratio \qquad (4-9)$$

In this calculation, the absorption ratio A was then calculated as:

$$A = 1 - T \qquad (4-10)$$

4.4 Result and Analysis

4.4.1 Anthracene

4.4.1.1 Experiment Result

In this experiment, more than ten anthracene samples were used for measurement. The four absorption spectra with error bars are shown in the figure, An un, AnK1h, AnK1.5h, and AnK3h.

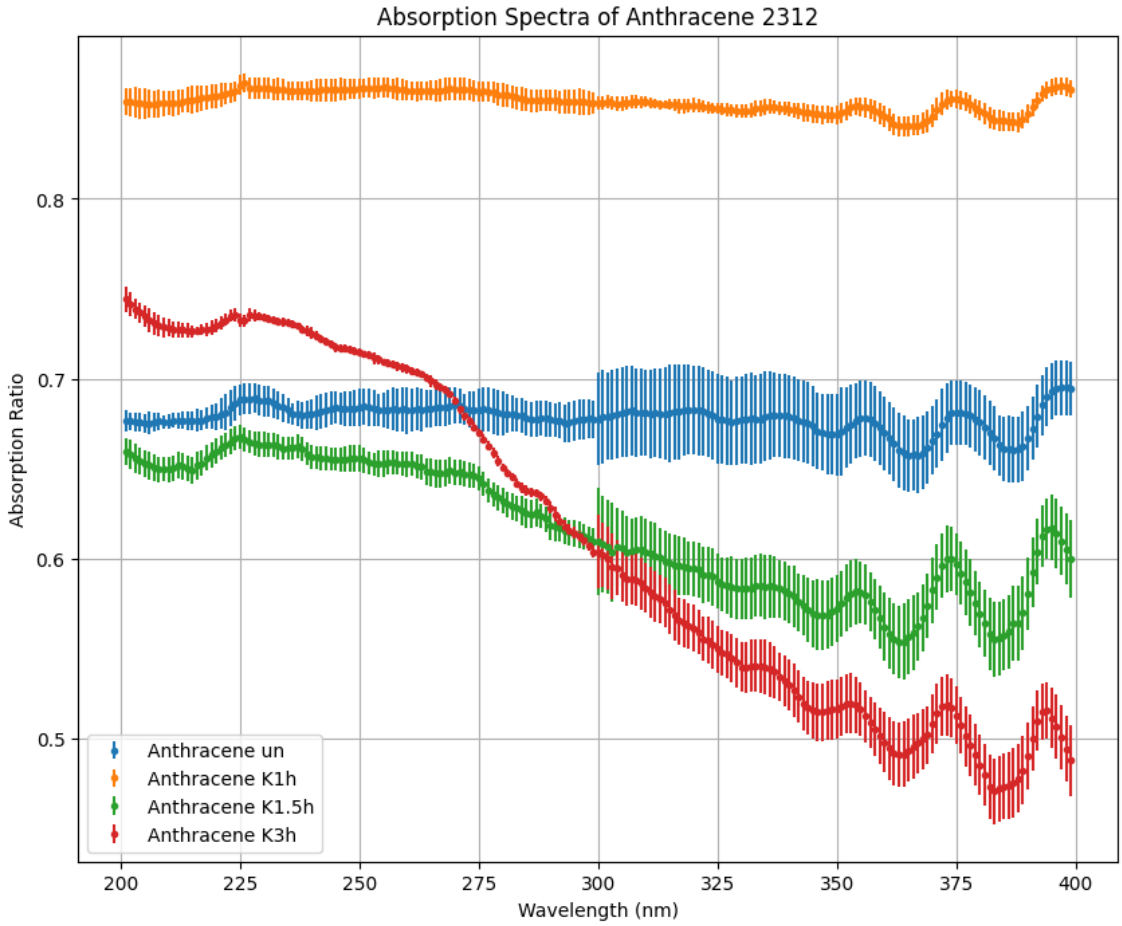

Figure 4.4.1 The Absorption Spectra of four anthracene samples.

Blue: Anun— the anthracene sample has not been irradiated.

Orange: AnK1h—the anthracene sample has been irradiated for 1 hour at Kashiwa using Deuterium Lamp.

Green: AnK1.5h—the anthracene sample has been irradiated for 1.5 hours at Kashiwa using Deuterium Lamp.

Blue: AnK3h—the anthracene sample has been irradiated for 3 hours at Kashiwa using Deuterium Lamp.

Considering the color, density, and coverage of grains and the sample thickness measurement results, the sample used for 1-hour irradiation has the thickest sample layer between the four samples. Therefore, the absorption ratio is the highest, as it can be seen from the orange line.

A bump around 225 nm can be seen in the absorption spectra of three thinner samples. This bump is possible due to the electronic transitions, which are π-π* transitions, a common kind of transitions in the UV range for PAHs like anthracene and coronene.

Continuous peaks from 300 nm to 400 nm can be observed. These peaks are possibly due to fluorescence, this suggests that the anthracene sample is exhibiting fluorescence emission in this wavelength range. When anthracene absorbs UV light, it can become excited to a higher electronic state. Upon returning to the ground state, it can emit light at longer wavelengths, which is observed as fluorescence.

To observe closely, the fluorescence spectrum in the range of 320 nm to 400 nm is magnified in the figure. A slight shift in the peak wavelengths is observable. As highlighted in the figure, the peak around 375 nm serves as a representative example, demonstrating a gradual shift to shorter wavelengths with increasing irradiation time. Specifically, for anthracene without irradiation, the peak is at 375 nm. After 1.5 hours of irradiation, the peak shifts to approximately 373-374 nm. Following 3 hours of irradiation, the peak further shifts to 372 nm.

An investigation and analysis were conducted to account for any potential discrepancies or offsets between the wavelength displayed by the beamline control system and the actual wavelength during measurements. The findings indicate that any offset in the measurement wavelength over time is negligible and falls below the resolution of the measurement, thus it can be disregarded.

UV irradiation may cause bond breakage or the formation of new bonds in anthracene molecules, altering their molecular structure, for instance, the loss of hydrogen. These structural changes can lead to changes in electronic energy levels, resulting in a blue shift (shift towards shorter wavelengths) in the fluorescence emission peaks.

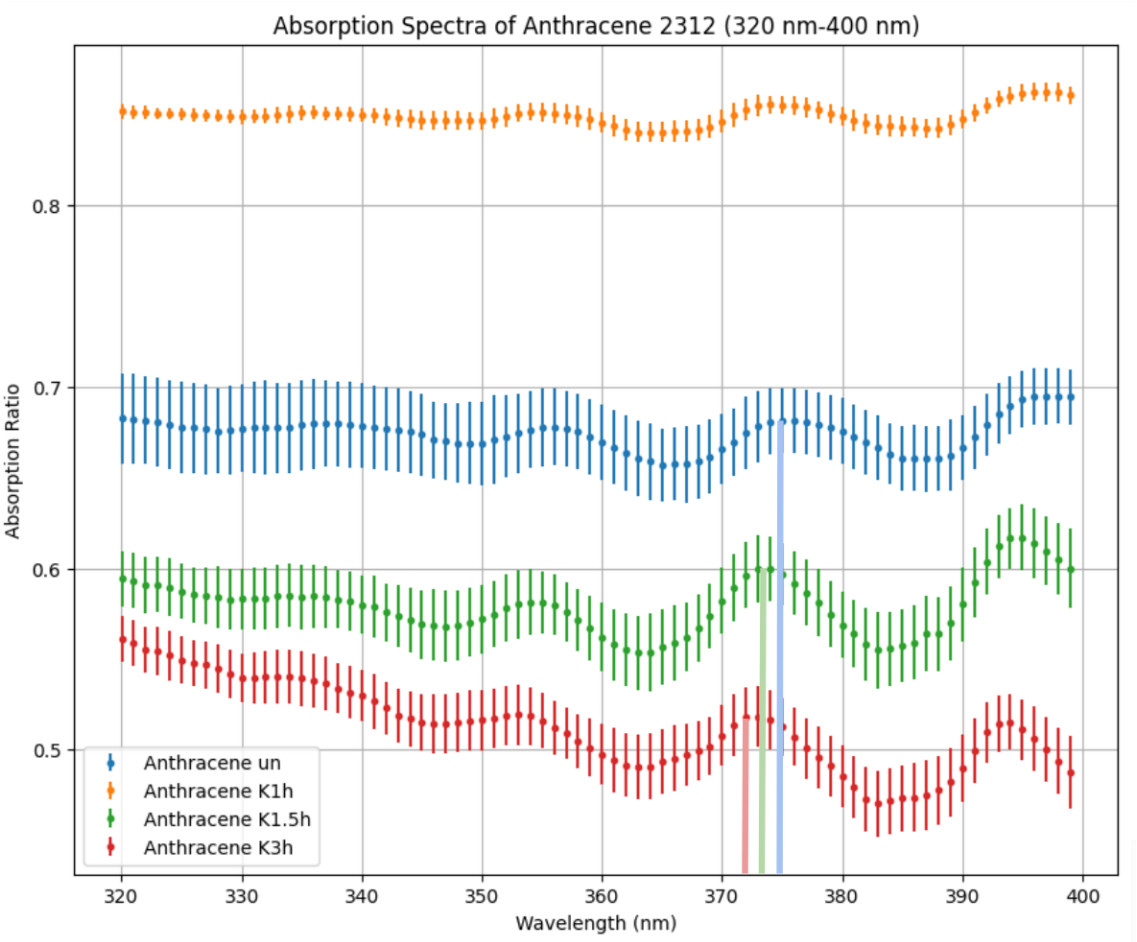

Figure 4.4.2 The Absorption Spectra of anthracene samples from 320 nm to 400 nm.

4.4.1.2 Comparison with Previous Research

Comparing experimental data with previous studies reveals a less prominent region from 200 to 300 nm in our research, whereas a distinct absorption peak at 250 nm is evident in the earlier study. This difference likely arises from the use of solid samples in our study, which are relatively thicker, compared to the organic solvent-based liquid samples used previously. Spectra measured in liquid form typically exhibit stronger transmission signals.

Furthermore, in the fluorescence spectrum range of 300 to 400 nm, our spectral data correspond well with previous research findings.

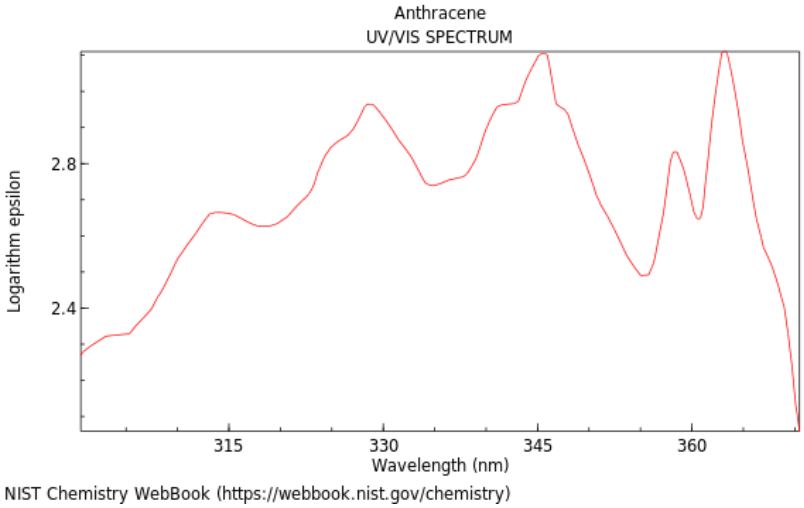

Figure 4.4.3 Computational Spectra of Anthracene from 300 nm to 370 nm. (Source: Database NIST)

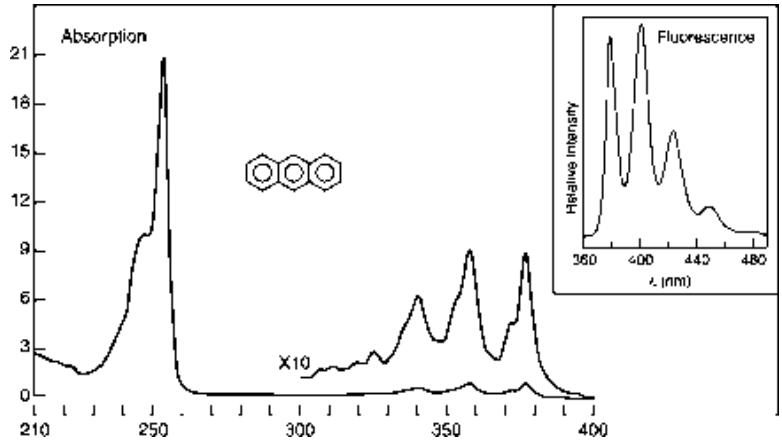

Figure 4.4.4 UV absorption and fluorescence spectra of anthracene in cyclohexane (adapted from Karcher et al., 1985). (from 210 nm to 400 nm).

It is worth noting that the experimental spectra and computational spectra do not completely align due to several factors. These include the choice of models during calculations, the idealized settings in computational software, potential impurities in experimental samples, and the influence of sample thickness for solids and the choice of organic solvents for liquid spectra. These factors will be further discussed in the next chapter: Computational Chemistry.

4.4.2 Coronene

4.4.2.1 Experiment Result

In this experiment, more than twenty coronene samples were used for measurement. The four absorption spectra with error bars are shown in the figure, Coronene un, Coronene U3h, Coronene U8h, and Coronene K12h.

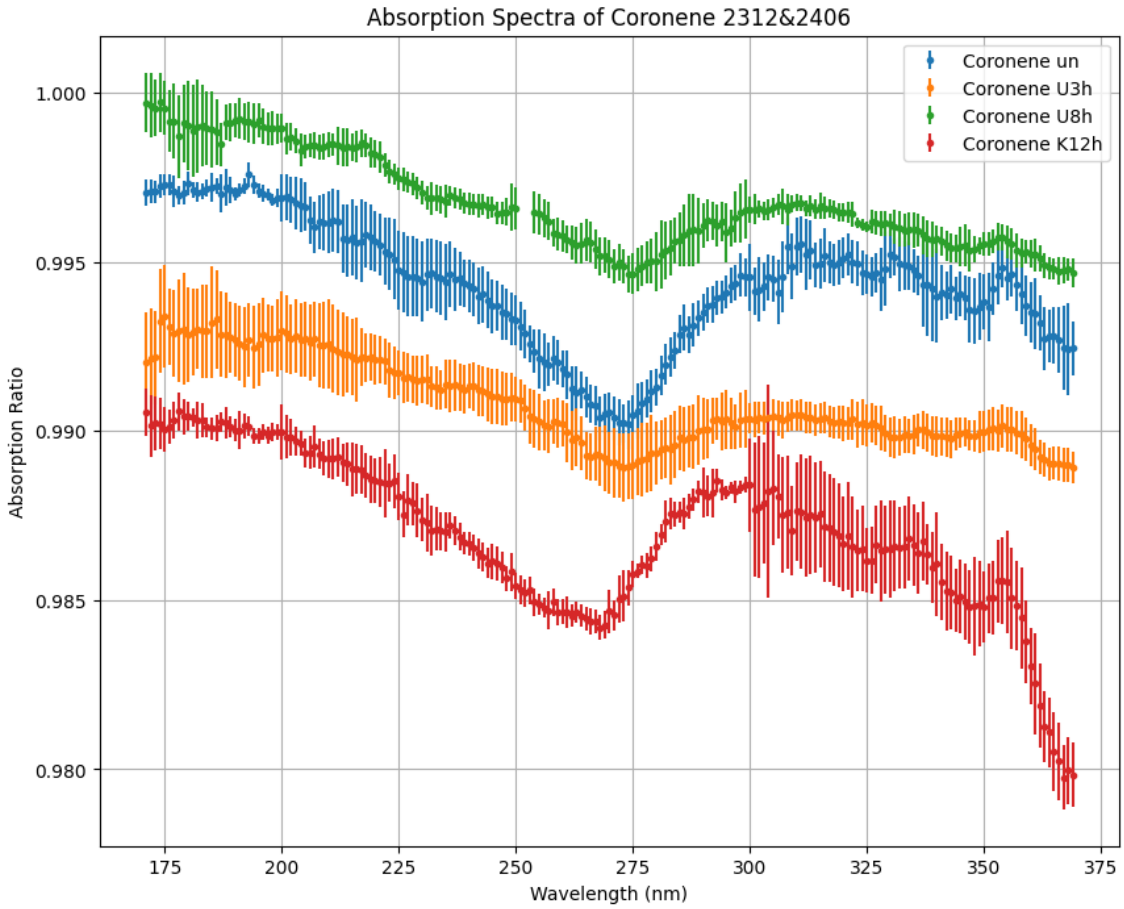

Figure 4.4.5.a Absorption spectra of coronene samples under different time irradiation

Blue: the coronene sample has not been irradiated at 23/12.

Orange: the coronene sample has been irradiated for 3 hours at UVSOR using 0th-order light at 24/06.

Green: the coronene sample has been irradiated for 8 hours at UVSOR using 0th-order light at 24/06.

Red: the coronene sample has been irradiated for 12 hours at Kashiwa using Deuterium Lamp at 23/12.

The thickness of the samples of 24/06 followed similar thickness level as the samples of 23/12. As is shown in the graph, the absorption ratio is similar and can be compared. Though, the peaks and valleys are less obvious at 24/06 samples.

Comparing with figure 4.4.7, which is an experimental result of coronene spectra under room temperature, a bump around 200 nm and a peak around 300 nm and a small peak(probably vibrational fine structure) can be seen.

A possible shift may exist at the peak around 300 nm observing the absorption spectra of coronene with no irradiation and coronene with 12 hours of deuterium arc lamp irradiation.

4.4.2.3 Running average for Smoothing

Exponential Weighted Moving Average is used in the smoothing of data. It generates a new data set by taking each data point in the data set and averaging it with the points before and after it. Most importantly it applies more weight to closer data points while giving less weight to further data points.

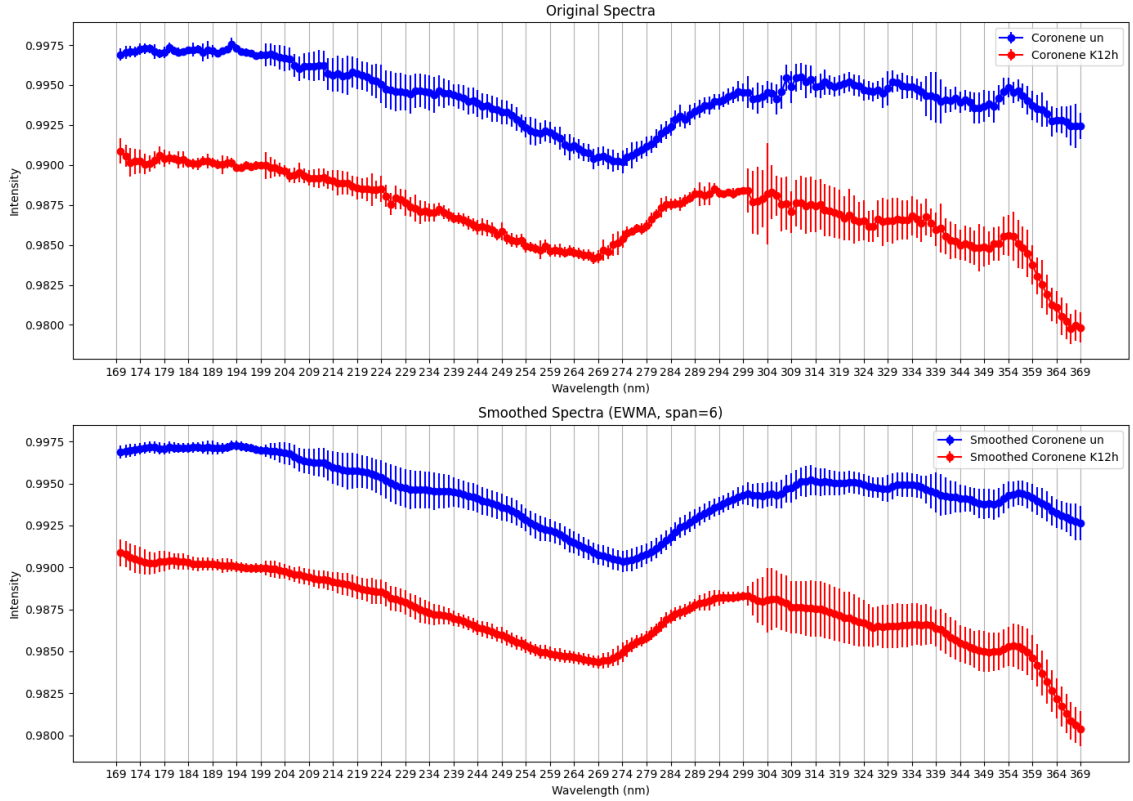

Figure 4.4.5.b Original Spectra and Smoothed Spectra comparison of Coronene un and Coronene K12h.

When comparing the valleys around λ=270 nm, a shift of about 5 nm can be observed, but when comparing λ=300 nm, the results show that while there appears to be a shift, no clear shift was observed with this level of UV irradiation.

4.4.2.3 Comparison with Previous Research

When comparing the calculated spectra from previous studies with experimental spectra, a strong absorption peak near 200 nm is observed in the former, which is less prominent in our research. Additionally, a relatively flat bump is seen from 170 nm to 220 nm in our data. The calculated spectra show a secondary absorption peak at 340 nm, while the experimental spectra exhibit this peak around 310 nm, along with a minor peak at 350 nm, possibly related to vibrational spectra. The bump around 300 nm appears in all samples, though the exact peak positions require further study for confirmation.

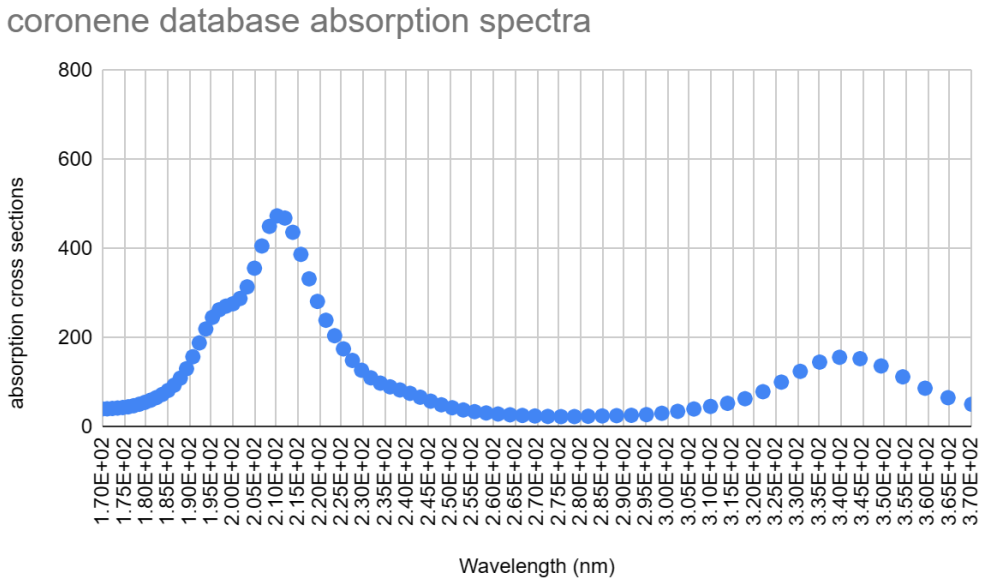

Figure 4.4.6 The computational absorption spectra of coronene from 170 nm to 370 nm in the database by G. Malloci and G. Mulas

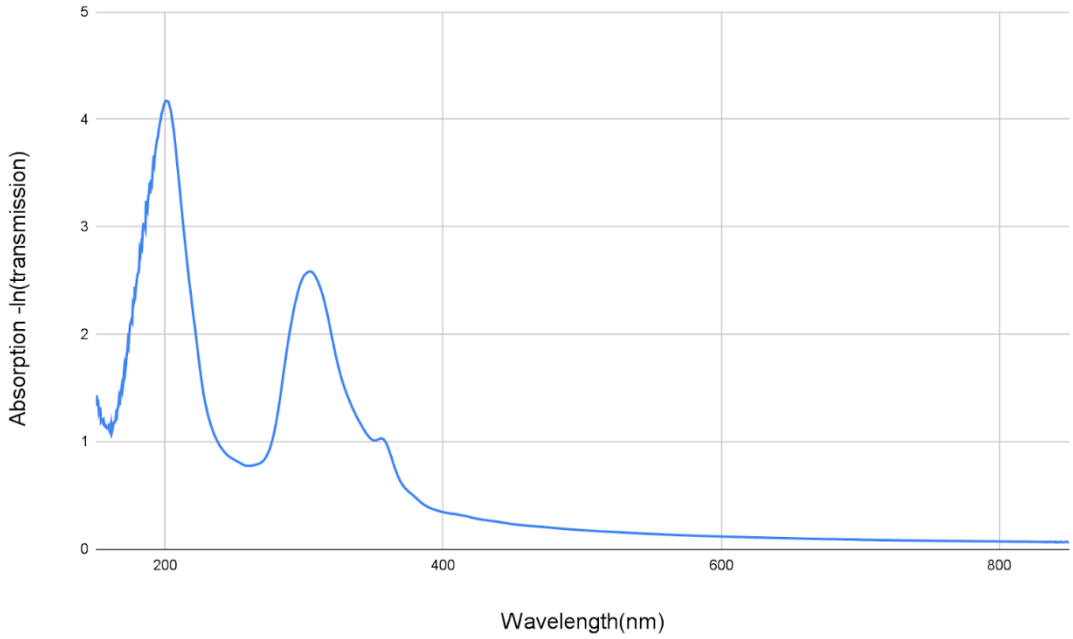

Figure 4.4.7 The experimental absorption spectra of coronene from 150 nm to 900 nm by M. Steglich 2011.

4.4.3 Error Analysis

4.4.3.1 Direct Intensity Analysis

Due to the structure of the BL7B beamline, the intensity of direct light exhibits temporal changes. One plausible explanation for this phenomenon is that the mirror within the beamline requires time to heat up. The fluctuation in temperature affects the mirror's reflectivity, thereby altering the intensity of the direct light. Although the synchrotron accelerator operates at a relatively stable current—around 200 mA during the experiments conducted in December 2023 and June 2024—the intensity of direct light increases as the mirror heats up. Preliminary investigations indicate that the final measurement of direct light intensity can be more than twice as large as the initial measurement.

To quantify this effect, the intensity of direct light was continuously monitored for 20 hours. The figure presents the direct light intensity measurements at 250 nm, with the data points representing the voltage output by the photodiode and the x-axis indicating the irradiation time. The presence of dark noise necessitated a calculation method analogous to that used in previous spectral measurements, with the final data averaged from three sets of measurements.

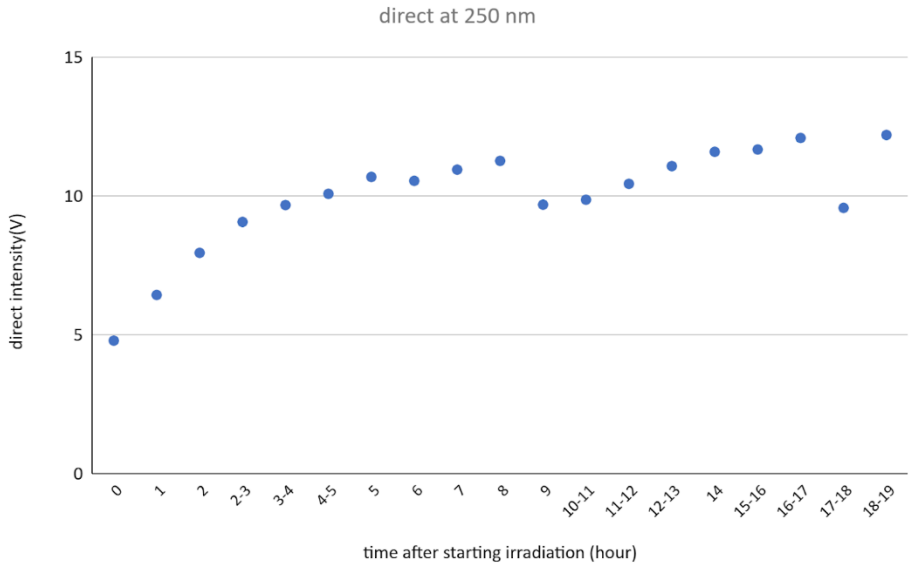

Figure 4.4.8 The direct intensity output voltage at 250 nm changes over time after hours starting irradiation

The figure reveals that the initial intensity measurement was approximately 5 volts, while the final measurement exceeded 12 volts. It is observed that the intensity significantly increases during the first 3 hours. Although fluctuations persist, the intensity tends to stabilize after 5-6 hours.

Based on these observations, it can be concluded that initiating measurements after the beamline has been operating for 6 hours may reduce errors attributable to the heating of the mirror, thereby enhancing the accuracy of the direct light intensity measurements.

4.4.3.2 Dark Noise Analysis

Dark noise is the data collected when the beam light is shut down, ideally resulting in no photons being received by the photodiode. However, due to potential light leaks in the optical path and, more importantly, the inherent dark noise of the photodiode and the preamplifier, it is essential to measure the dark noise.

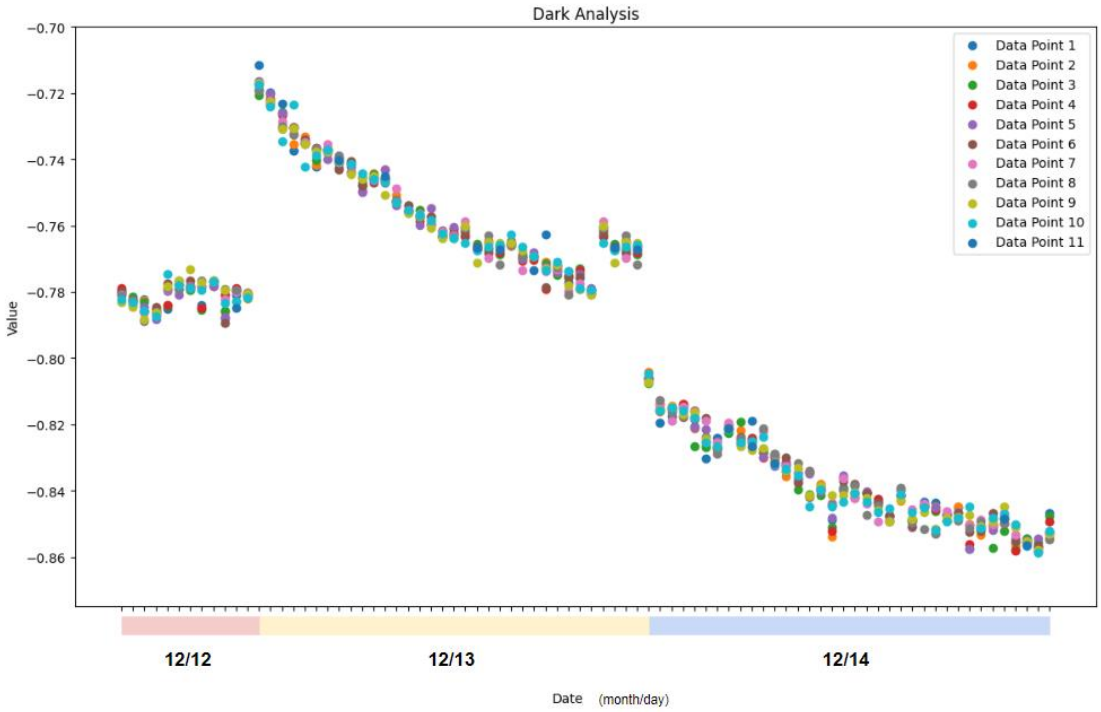

Figure 4.4.9 The dark current intensity output voltage changes over time in three days of measurement (2023/12/12, 2023/12/13, 2023/12/14).

In this investigation, dark noise was measured continuously over several days (December 12, 2023; December 13, 2023; and December 14, 2023). Each vertical set of data

represents a set of spectral measurements, where the 11 data points in each set correspond to the average values of 11 dark noise measurements.

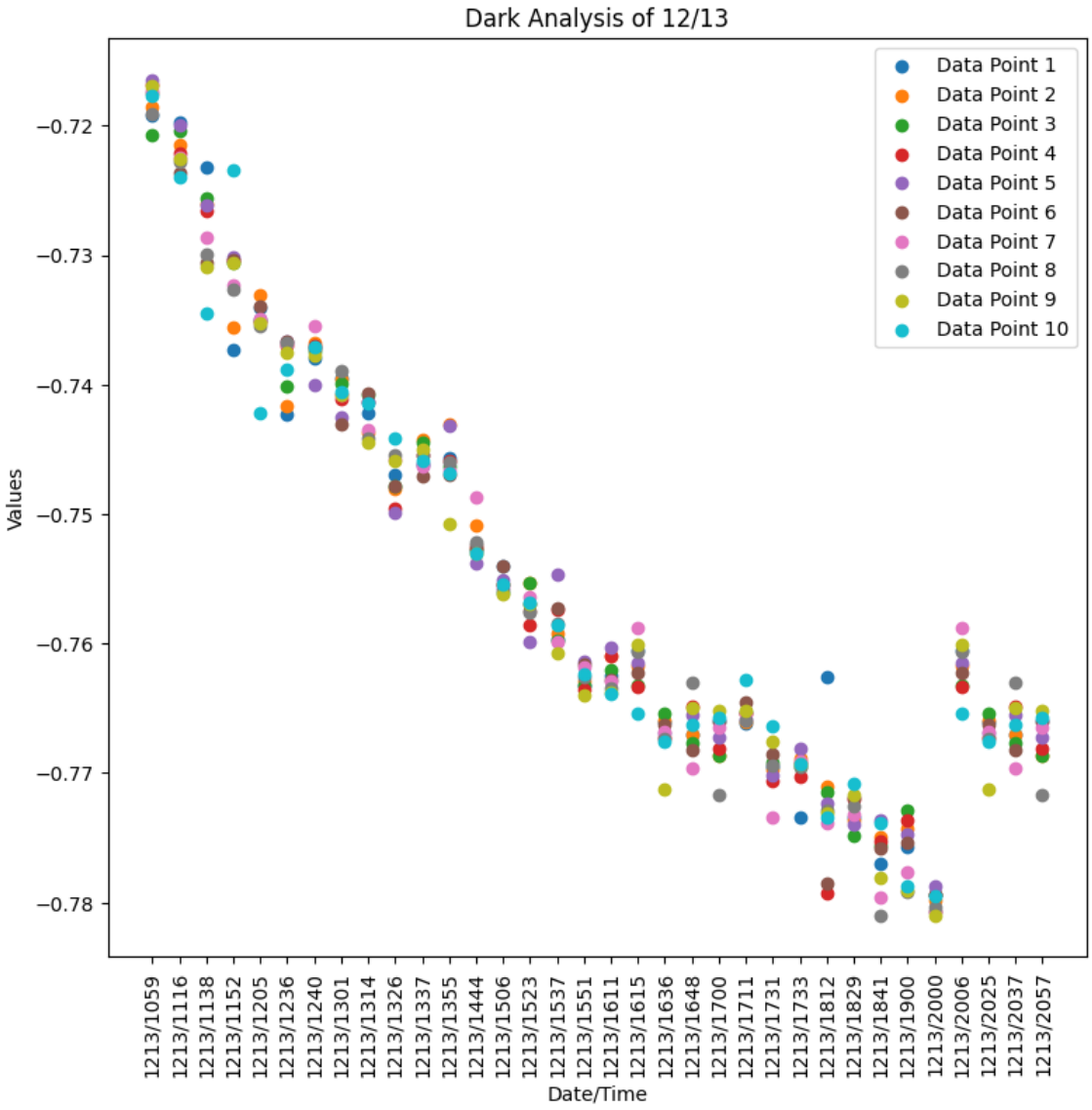

Figure 4.4.9 The dark current intensity output voltage changes over time at 2023/12/13.

The data indicates that the value of dark noise increases continuously. As shown in the measurements from December 13, a gap appears between measurements 1213/2000 and 1213/2006, which is attributed to a restart of the amplifier. Despite this restart, the dark noise continued to increase, and there was no change in the value after turning off the power supply for one minute.

Two possible causes may explain the fluctuation in dark noise. Firstly, it may result from the accumulation of charge being read out, as evidenced by the decrease in dark current after a reset. Secondly, continuous exposure to light may lead to an increase in dark current, as the dark current continues to increase with a similar trend over time.
By carefully monitoring and analyzing these factors, the investigation aims to understand better and mitigate the impacts of dark noise on the accuracy of the experimental measurements.

4.4.3.3 Wavelength Offset Analysis

A potential source of error in the measurement may arise from drift or offset in the wavelength calibration. This discrepancy occurs when the indicated wavelength displayed by the beamline's computer and controlling system deviates slightly from the actual wavelength of the light. However, the cutoff wavelength of specific materials remains constant under identical measurement conditions. These materials exhibit a sudden change in transmittance within the UV range, which can be utilized for calibration purposes. By identifying the exact wavelength at which this abrupt change occurs, it is possible to calculate the difference between the indicated and actual wavelengths. Consequently, investigating the cutoff wavelength is essential for ensuring accurate measurements.
In this study, the spectral measurements span from 170 nm to 400 nm, primarily employing the G3 grating of the beamline. To ensure accurate wavelength calibration, measurements of the cutoff wavelength were conducted using the G3 grating in conjunction with Quartz and Pyrex filters with the thickness of 1mm. This approach allows for precise determination of the wavelength offset, thereby enhancing the reliability of the experimental results.

- Quartz

Quartz shows a cutoff frequency of around 155 nm. This is similar to the data measured at UVSOR beamline BL7B. In this case, it can be deduced that there is no significant shift or offset.

Additionally, it can be observed that different measurement times show no significant change in the cutoff frequency. Consistent results were obtained from measurements conducted over five days in December 2023 and June 2024.

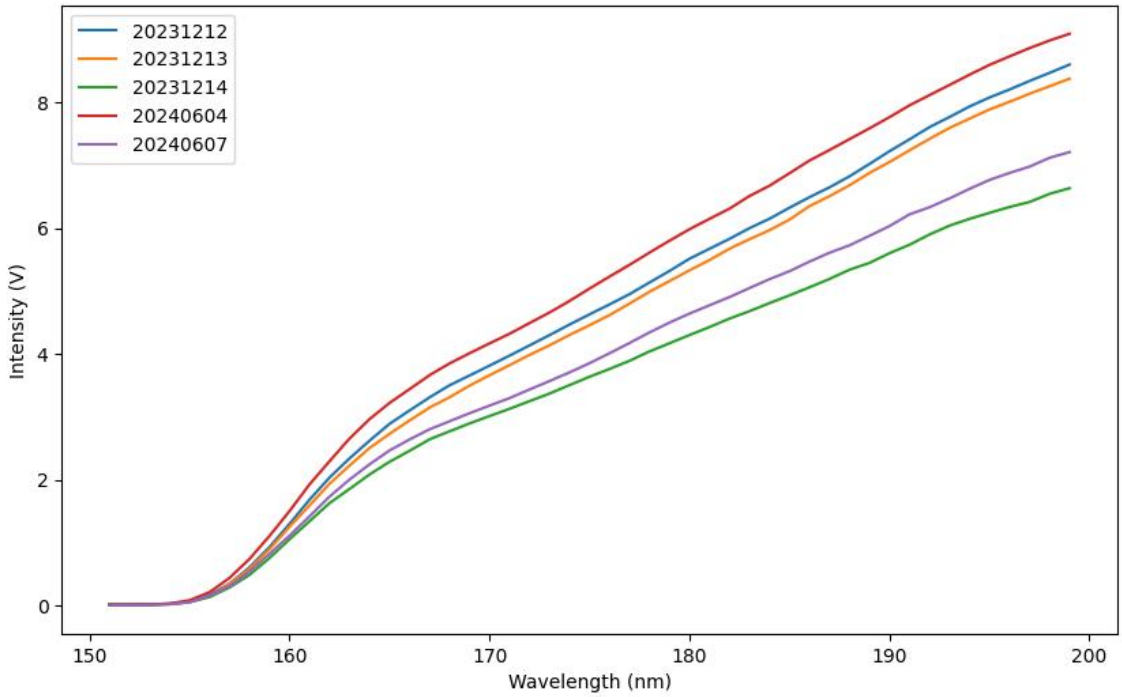

Figure 4.4.10.a The direct intensity measured using Quartz filter.

The original intensity data from various days were visualized against the wavelength data, followed by logarithmic linear regression.

For simplicity of expression:
B: 20231212
C: 20231213
D: 20231214
E: 20240604
F: 20240607

The logarithmic linear regression results are as follow,

log(C) = 1.03log(B) + -0.08, r^2 = 1.00
log(D) = 1.00log(B) + -0.24, r^2 = 1.00
log(E) = 1.03log(B) + 0.06, r^2 = 1.00
log(F) = 1.06log(B) + -0.26, r^2 = 1.00

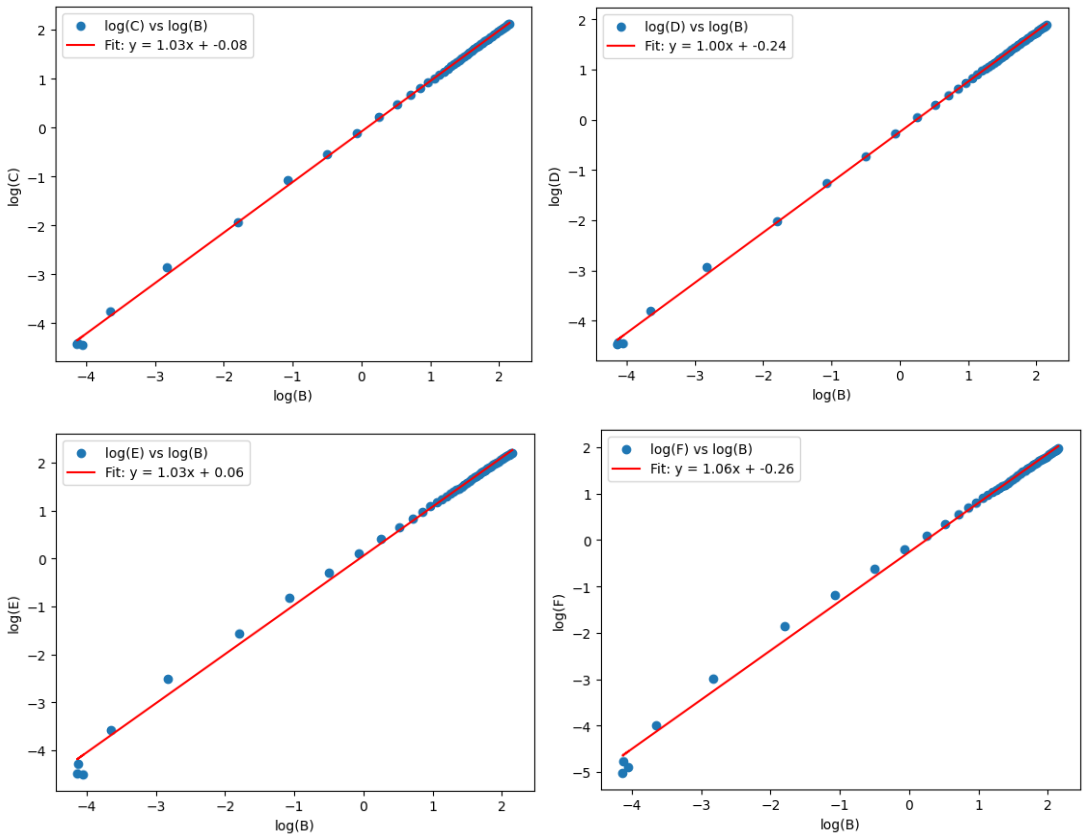

Figure 4.4.10.b The linear regression analyses of B vs C, B vs D, B vs E, B vs F.

The analysis revealed near-perfect linear relationships in the logarithmic space, with slopes close to 1 and R^2 values of 1.00, indicating that the datasets are nearly identical, with primary differences attributable to scaling factors.

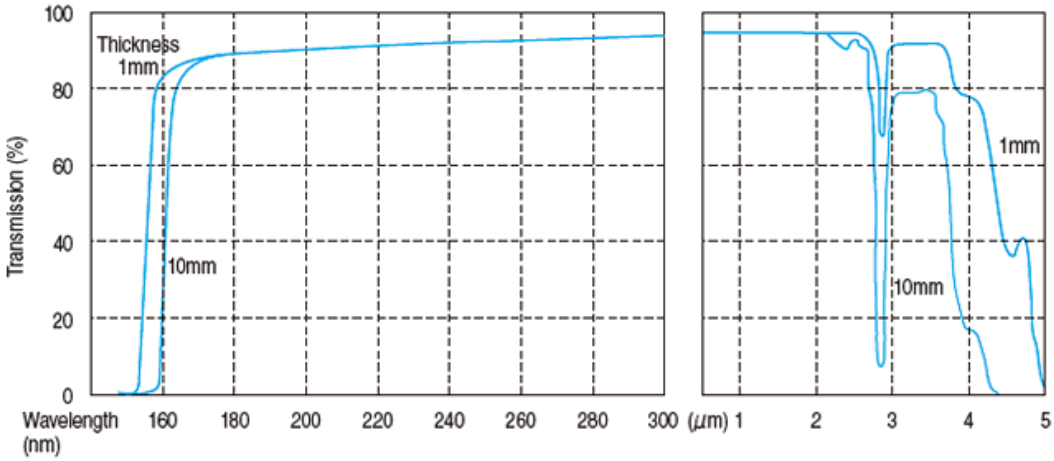

Figure 4.4.10.c Quartz transmission of thickness 1mm and 10mm (Source: Ohara Quartz, n.d.).

- Pyrex

Pyrex shows a cutoff frequency of around 250 nm. This is similar to the data measured at UVSOR beamline BL7B. In this case, it can be deduced that there is no significant shift or offset.

Similarly, in the Pyrex measurements, the cutoff wavelength remained consistent across different measurements conducted over four days in December 2023 and June 2024.

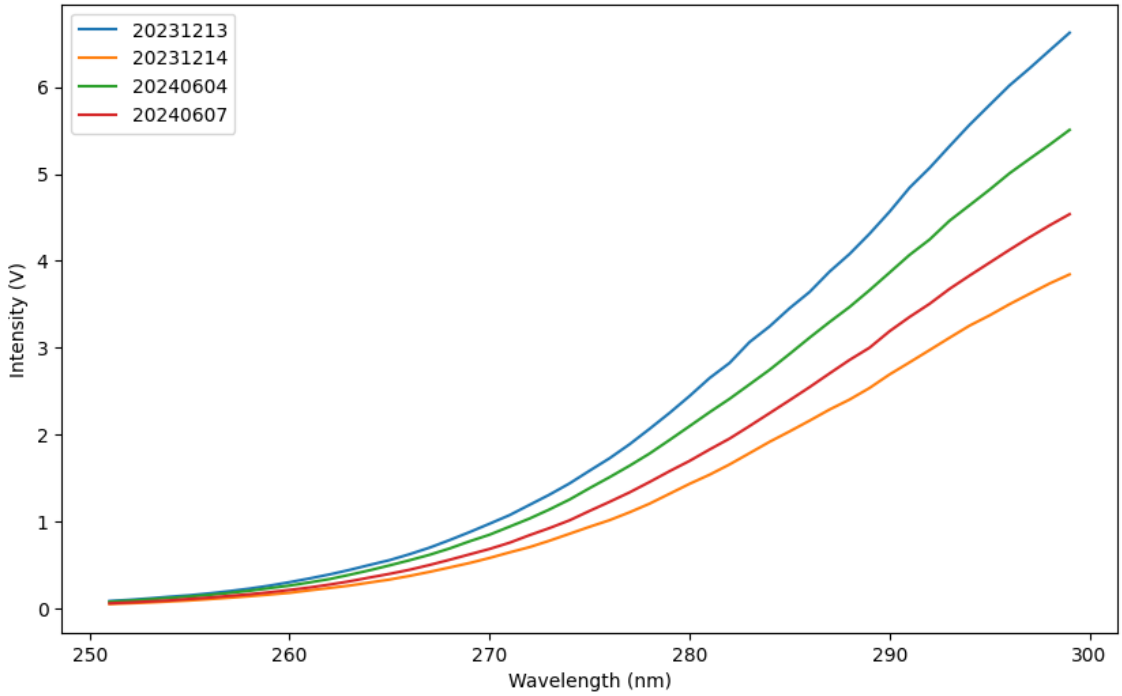

Figure 4.4.11.a The direct intensity measured using Pyrex filter.

A similar analysis was also performed on the Pyrex cutoff frequency data.

These datasets also exhibit near-perfect linear relationships in the logarithmic space with slopes close to 1 and R^2 values of 1.00, indicating they are nearly identical with primary differences due to scaling factors.

For simplicity of expression:

I: 20231213

J: 20231214

K: 20240604

L: 20240607

The logarithmic linear regression results are as follow,

log(J) = 1.03log(I) + -0.08, r^2 = 1.00

log(K) = 1.00log(I) + -0.24, r^2 = 1.00

log(L) = 1.03log(I) + 0.06, r^2 = 1.00

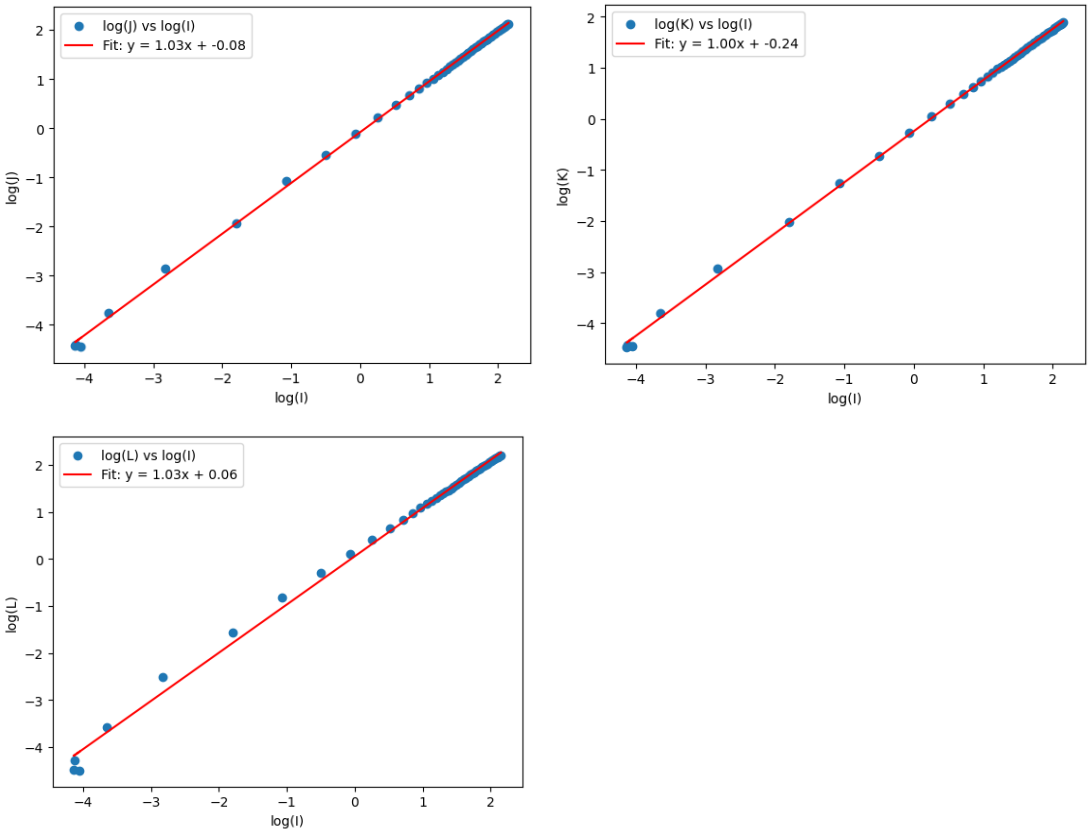

Figure 4.4.11.b The linear regression analyses of I vs J, I vs K, I vs L.

The analysis also exhibited near-perfect linear relationships in the logarithmic space, with slopes close to 1 and R^2 values of 1.00, indicating that the datasets are nearly identical, with primary differences attributable to scaling factors.

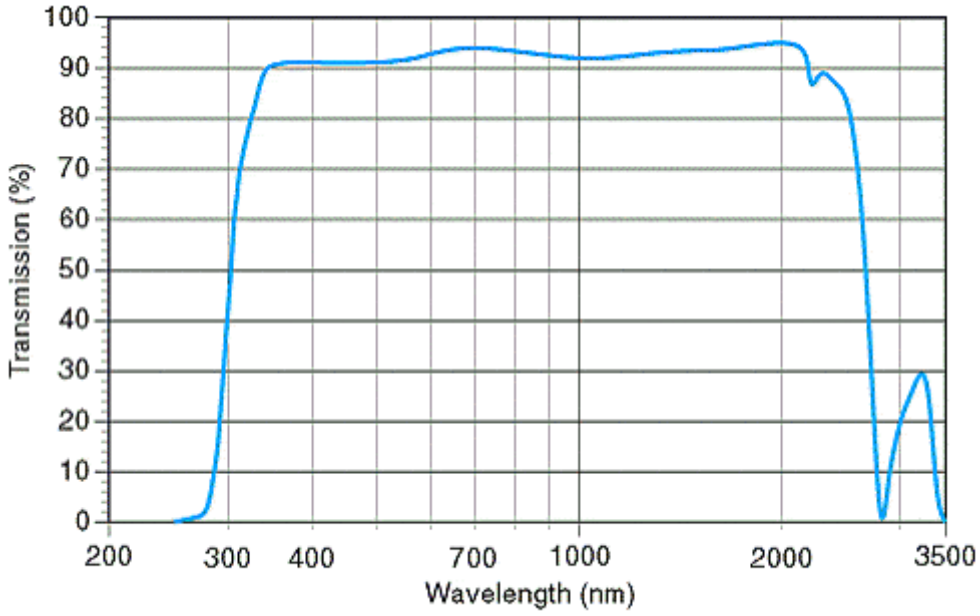

Figure 4.4.11.c Pyrex transmission of thickness 1 mm (Source: American Scientific Glassblowers Society).

4.4.3.4 Error Bar Calculation

As is mentioned in the data structure section, each set of data includes specific types of data: dark noise (dark), direct light (direct), and transmitted light (trans). The sequence of data is as follows: dark_1, direct_1, dark_2, direct_2, dark_3, trans_1, dark_4, trans_2, dark_5, trans_3, dark_6, direct_3, dark_7, direct_4, dark_8. The goal is to calculate the measurement errors for each type of data and subsequently determine the transmission and absorption ratios along with their associated errors.

Step 1: Calculating the Errors for Direct-Dark and Trans-Dark Measurements

The errors for the direct-dark and trans-dark measurements were calculated by propagating the errors of the individual direct, trans, and dark measurements. The errors for the averages were computed using standard error propagation techniques.

For direct-dark measurements:

$$\sigma_{dark_{1,2}} = \sqrt{\left(\frac{\sigma_{dark_1}}{2}\right)^2 + \left(\frac{\sigma_{dark_2}}{2}\right)^2} \quad (4-11)$$

$$\sigma_{direct-dark_1} = \sqrt{\sigma_{direct_1}^2 + \sigma_{dark_{1,2}}^2} \quad (4-12)$$

Similar calculations were performed for the other direct-dark and trans-dark measurements.

The errors for the averages were then calculated as:

$$\sigma_{direct\_dark\_average} = \sqrt{\frac{\sigma_{direct-dark_1}^2 + \sigma_{direct-dark_2}^2 + \sigma_{direct-dark_3}^2 + \sigma_{direct-dark_4}^2}{4^2}} \quad (4-13)$$

$$\sigma_{trans\_dark\_average} = \sqrt{\frac{\sigma_{trans-dark_1}^2 + \sigma_{trans-dark_2}^2 + \sigma_{trans-dark_3}^2}{3^2}} \quad (4-14)$$

Step 2 Calculating the Errors for the Transmission and Absorption Ratios

The error in the transmission ratio was calculated using the propagation of errors formula:

$$\sigma_T = T \cdot \sqrt{\left(\frac{\sigma_{trans\_dark\_average}}{trans\_dark\_average}\right)^2 + \left(\frac{\sigma_{direct\_dark\_average}}{direct\_dark\_average}\right)^2} \qquad (4-15)$$

Since A=1−T, the error in the absorption ratio is the same as the error in the transmission ratio:

$$\sigma_A = \sigma_T \qquad (4-16)$$

5. Computational Chemistry

5.1. Introduction

Computational chemistry is a field of chemistry that uses computer simulation to assist in solving chemical problems. It employs theoretical chemistry methods implemented in computer software to calculate the properties and behaviors of molecules and materials. The foundational theories behind computational chemistry include quantum mechanics and classical mechanics, particularly through methods like Density Functional Theory (DFT), Time-Dependent Density Functional Theory (TD-DFT), and Hartree-Fock (HF). At the core of computational chemistry is quantum mechanics, which describes the behavior of electrons in atoms and molecules. The Schrödinger equation is fundamental, providing a mathematical description of how the quantum state of a physical system changes over time.

DFT is widely used for calculating the electronic structure of molecules and materials. It simplifies the many-body problem of interacting electrons using the electron density rather than the many-electron wavefunction. Based on the DFT method, TD-DFT extends DFT to study the excited states of molecules, allowing for the simulation of electronic spectra by calculating excitation energies and transition probabilities.

5.2. Calculation

Computational chemistry can simulate the spectra of molecules by calculating the electronic transitions between different energy levels. The main steps include:

- Geometric Optimization: Determining the most stable structure of the molecule.
- Electronic Structure Calculation: Using DFT or HF methods to find the ground state electron distribution.
- Excited State Calculation: Using TD-DFT or other methods to calculate the energies of excited states and their transition probabilities.

These calculated transitions correspond to the absorption or emission of light at specific wavelengths, which forms the basis for simulating UV-Vis, IR, or other types of spectra. In the experiment of UV-vis spectra simulation, two computational software, Gaussian and PySCF, were used to calculate the spectra of coronene.

Gaussian is a widely used commercial computational chemistry software that supports various quantum chemical methods. (The computation by Gaussian was conducted using National Computational Infrastructure in Australia under the guidance of Dr Rika Kobayashi, who is an academic consultant at Australian National University.)

PySCF (Python-based Simulations of Chemistry Framework) is an open-source computational chemistry software designed for flexibility and extensibility. (The computation by PySCF was conducted using Google Colab.)

5.3. Analysis

5.3.1 Gaussian

Figure 5.1 represents the UV-Vis spectrum of coronene, calculated using Gaussian software. The spectrum covers the range from approximately 100 nm to 500 nm.

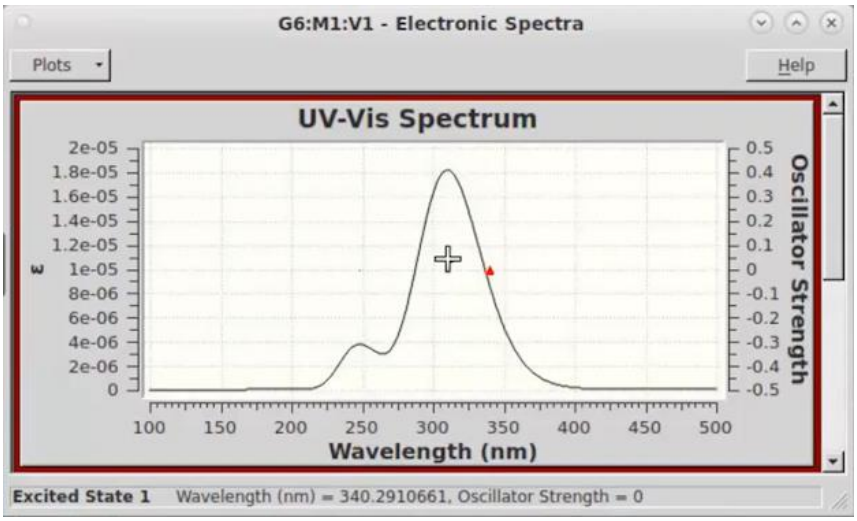

Figure 5.1 Coronene UV-vis spectra Simulation Result using Gaussian

The most prominent absorption peak occurs around 310 nm, which is indicated by the cursor in the plot. This peak is significant, showing a high oscillator strength, suggesting a strong electronic transition in this region.

There is also a smaller peak around 250 nm, indicating another electronic transition but with lower intensity compared to the main peak at 310 nm.

The peak at 340 nm can be attributed to π-π* electronic transitions, which are typical for conjugated systems like PAHs such as coronene.

The smaller peak at 250 nm also represents π-π* transitions but involves different molecular orbitals or transitions.

The oscillator strength is a measure of the probability of the transition. The higher the oscillator strength, the more likely the transition. The main peak at 340 nm has a high oscillator strength, indicating a highly probable electronic transition.

5.3.2 PySCF

Figure 5.2 represents the UV-vis spectrum of coronene, calculated using the PySCF computational chemistry software. The spectrum spans from approximately 180 nm to 350 nm. There are two significant peaks observed, a smaller peak around 200 nm and a much larger peak around 280 nm, which is the most prominent feature in the spectrum.

The peak around 280 nm likely corresponds to the π-π* electronic transition within the coronene molecule. The smaller peak around 200 nm might represent higher energy π-π* transitions.

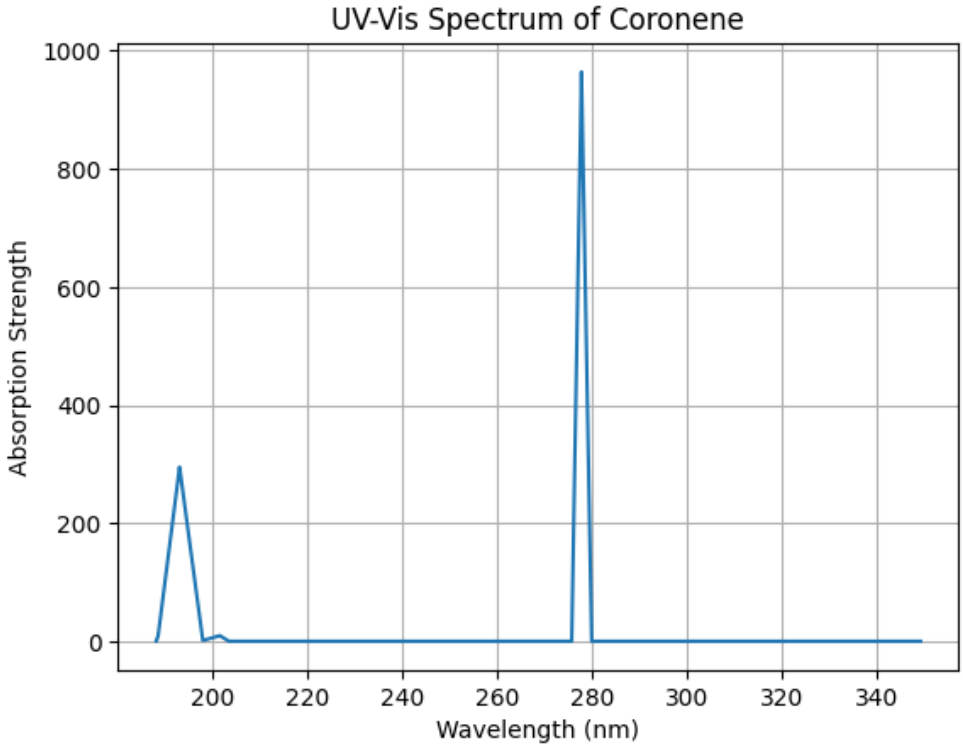

Figure 5.2 Coronene UV-vis spectra Simulation Result using PySCF

5.3.3 Comparative Analysis

In similarities, both Gaussian and PySCF use the TD-DFT method to compute the UV-Vis spectra of coronene. Both the calculation results show two significant peaks, one secondary higher energy peak and one main peak around 310 nm. Both reflect the characteristic π-π* electronic transitions typical of aromatic compounds.

In differences, compared to the Gaussian-calculated spectrum, the PySCF spectrum shows a significant absorption peak at a shorter wavelength (280 nm) rather than the 310 nm peak observed with Gaussian. This discrepancy could be due to differences in the parameter settings, basis sets, or levels of theory used in the two software packages.

Comparing computationally derived spectra with experimental results often reveals discrepancies due to several factors. Firstly, computational chemistry software typically calculates spectra for a single molecule in an ideal, isolated condition, whereas experimental samples are usually thicker and involve more complex interactions. Secondly, experimental measurements can be affected by noise, calibration issues, and resolution limitations, factors that are not accounted for in computational models. These differences highlight the inherent complexities and limitations of both computational and experimental approaches in accurately predicting and measuring spectra.

5.4 Conclusion

In this chapter, the use of computational chemistry to simulate the UV-Vis spectra of coronene, a polycyclic aromatic hydrocarbon (PAH), was explored fundamentally. Time-Dependent Density Functional Theory (TD-DFT) was employed using two software packages, Gaussian and PySCF, to compute excitation energies and oscillator strengths. Significant differences in peak positions and absorption intensities were observed, highlighting the impact of basis sets, functionals, and computational parameters.

For future work, systematic benchmarking using identical settings across multiple software packages should be conducted to identify sources of discrepancies. Additionally, new functionals and basis sets should be explored to enhance the accuracy and efficiency of TD-DFT calculations.

6. Conclusion

This study provides significant insights into the effects of space weathering on polycyclic aromatic hydrocarbons (PAHs), specifically focusing on the UV-induced changes in anthracene and coronene. Through controlled laboratory simulations using UV irradiation in a vacuum environment, we have observed distinct behaviors and transformations in these PAH molecules.

Firstly, anthracene exhibited noticeable fragmentation and evaporation during the irradiation process, particularly under the deuterium arc lamp, indicating a high susceptibility to photodissociation. In contrast, coronene, due to its larger molecular size and structural stability, showed no significant decomposition under similar conditions. This suggests that the molecular weight and stability of PAHs play crucial roles in their response to UV irradiation. The fragmentation of anthracene under the deuterium lamp suggests that a layer of anthracene with a thickness between 10 to 100 μm could decompose or evaporate within approximately three months under 1 AU solar irradiance.

Moreover, both anthracene and coronene samples demonstrated a shift in their UV absorption peaks towards shorter wavelengths after irradiation. This spectral shift, coupled with mass spectrometry data, points to the photodissociation of PAHs as a likely cause. These findings highlight the impact of space weathering on the chemical and physical properties of PAHs, potentially influencing their spectral signatures observed in astrophysical environments.

The results of this study contribute to a deeper understanding of the alteration mechanisms of PAHs under space weathering conditions. Future research could explore a broader range of PAH molecules and more diverse space weathering processes to further elucidate the complex interactions and transformations occurring in space.

In conclusion, this research underscores the importance of laboratory simulations in studying the dynamic processes affecting PAHs in space. By enhancing our knowledge of these processes, we can better comprehend the evolution and role of PAHs in various astrophysical contexts, contributing to the broader field of astrochemistry as well as astrobiology and the understanding of the origin of life in the universe.

Acknowledgements

I wish to express my most profound appreciation to my supervisor, Professor Ichiro Yoshikawa, for his insightful guidance and continuous support throughout my master's course. Discussions with him have always been fruitful.

I would also like to express my sincere appreciation to Associate Professor Itsuki Sakon from the Department of Astronomy for his invaluable advice and assistance with my experiments.

My heartfelt thanks go to Lecturer Kazuo Yoshioka, Professor Takeshi Imamura and Lecturer Shohei Aoki, for their kind encouragement and valuable comments.

Part of the work presented in Chapter 3 and Chapter 4 was performed at the BL7B of the UVSOR Synchrotron Facility, Inst. Mol. Sci. Okazaki. I have greatly benefited from Mr. Eiken Nakamura and Mr. Naonori Kondo, the technical staff at UVSOR.

Another part of the work in Chapter 5 was performed under the guidance of Dr. Rika Kobayashi, Academic Consultant of the Supercomputer Facility at Australian National University at NCI. I am grateful for her guidance in using Gaussian.

A special thanks to my senior Mr. Kazuki Inoue, for his guidance in PAH experiments and the vacuum system. My gratitude also extends to Mr. Chongming Wu for his contributions to my experiments and discussions about PAHs. I also thank my seniors, Mr. Shunichiro Teramoto, Mr. Ashita Yamazaki and Mr. Tatsuki Matsumoto, for their guidance and help with experiments.

I extend my thanks to my fellow lab mates in the Astrobiology Group of Yoshikawa-Yoshioka Lab and Imamura-Aoki Lab: Dr. Shota Chiba, Mr. Tatsuro Iwanaka, Ms. Miyu Sugiura, Mr. Gaku Kinoshita, Ms. Saniya Sanada, Ms. Suomi Seki, Mr. Xuanchao Fu, Mr. Zhengze Li, Mr. Huiyang Lin, Ms. Jie Yang, Ms. Mengtong Zhang for the stimulating discussions and all the knowledge we have shared over the past two years.

I am deeply grateful to Ms. Yueyao Dong of UCL for her kind support and suggestions to the experiments from eight time zones away.

My sincere thanks go to Designer Takaharu Suzuki for his assistance in designing illustrations for this thesis and for supporting me and my research.

I wish to express my deepest gratitude to my family, my cat, and my dog, for their priceless financial and emotional support.

Last but not least, I would like to thank myself, for finishing this thesis and recovering health after the surgery.

References

[1] Tielens, A. G. G. M. (2013). The molecular universe. *Reviews of Modern Physics*, *85*(3), 1021-1081.

[2] Fitzpatrick, E. L. (2004, May). Interstellar Extinction in the Milky Way Galaxy. In Astrophysics of Dust (Vol. 309, p. 33).

[3] Stecher, T. P., & Donn, B. (1965). On graphite and interstellar extinction. Astrophysical Journal, 142, p. 1681, 1965., 142, 1681.

[4] Mathis, J. S., Rumpl, W., & Nordsieck, K. H. (1977). The size distribution of interstellar grains. Astrophysical Journal, Part 1, vol. 217, Oct. 15, 1977, p. 425-433. NSF-supported research., 217, 425-433.

[5] Mathis, J. S. (1996). Dust models with tight abundance constraints. The Astrophysical Journal, 472(2), 643.

[6] Ferriere, K. M. (2001). The interstellar environment of our galaxy. Reviews of Modern Physics, 73(4), 1031.

[7] Schnaiter, M., Mutschke, H., Dorschner, J., Henning, T., & Salama, F. (1998). Matrix-isolated nano-sized carbon grains as an analog for the 217.5 nanometer feature carrier. The Astrophysical Journal, 498(1), 486.

[8] Steglich, M., Jäger, C., Rouillé, G., Huisken, F., Mutschke, H., & Henning, T. (2010). Electronic spectroscopy of medium-sized polycyclic aromatic hydrocarbons: implications for the carriers of the 2175 Å UV bump. The Astrophysical Journal Letters, 712(1), L16.

[9] Sarah S. Zeichner et al. ,Polycyclic aromatic hydrocarbons in samples of Ryugu formed in the interstellar medium. Science 382, 1411-1416(2023). DOI:10.1126/science.adg6304

[10] M., S., Murga., Vitaly, Akimkin., Dmitri, Wiebe. (2022). Efficiency of the top-down PAH-to-fullerene conversion in UV irradiated environments. Monthly Notices of the Royal Astronomical Society, 517(3):3732-3748. doi: 10.1093/mnras/stac2926

[11] Lemmens, A. K., Rap, D. B., Brünken, S., Buma, W. J., & Rijs, A. M. (2022). Polycyclic aromatic hydrocarbon growth in a benzene discharge explored by IR-UV action spectroscopy. Physical Chemistry Chemical Physics, 24(24), 14816-14824.

[12] Banhatti, S., Rap, D. B., Simon, A., Leboucher, H., Wenzel, G., Joblin, C., ... & Brünken, S. (2022). Formation of the acenaphthylene cation as a common C 2 H 2-loss fragment in dissociative ionization of the PAH isomers anthracene and phenanthrene. Physical Chemistry Chemical Physics, 24(44), 27343-27354.

[13] Joblin, C., Léger, A., & Martin, P. (1992). Contribution of polycyclic aromatic hydrocarbon molecules to the interstellar extinction curve. Astrophysical Journal, Part 2-Letters (ISSN 0004-637X), vol. 393, no. 2, July 10, 1992, p. L79-L82., 393, L79-L82.

[14] Papoular, R., Guillois, O., Nenner, I., Perrin, J. M., Reynaud, C., & Sivan, J. P. (1995). On the nature of interstellar carbonaceous dust. Planetary and Space Science, 43(10-11), 1287-1291.

[15] Moroz, L. V., Starukhina, L. V., Rout, S. S., Sasaki, S., Helbert, J., Baither, D., ... & Hiesinger, H. (2014). Space weathering of silicate regoliths with various FeO contents: New insights from laser irradiation experiments and theoretical spectral simulations. Icarus, 235, 187-206.

[16] Kimura, T., Otsuki, M., Kitano, T., Hoshino, R., Nakauchi, Y., Haganuma, S., ... & Miyake, Y. (2023). A plasma irradiation system optimized for space weathering of solar system bodies. Earth, Planets and Space, 75(1), 150.

[17] Sasaki, S., Nakamura, K., Hamabe, Y., Kurahashi, E., & Hiroi, T. (2001). Production of iron nanoparticles by laser irradiation in a simulation of lunar-like space weathering. Nature, 410(6828), 555-557.

[18] Loeffler, M. J., Dukes, C. A., & Baragiola, R. A. (2009). Irradiation of olivine by 4 keV He+: Simulation of space weathering by the solar wind. Journal of Geophysical Research: Planets, 114(E3).

[19] Gueymard, C. A. (2004). The sun's total and spectral irradiance for solar energy applications and solar radiation models. Solar energy, 76(4), 423-453.

[20] White, O. R., Rottman, G. J., & Livingston, W. C. (1990). Estimation of the solar Lyman alpha flux from ground based measurements of the Ca II K line. Geophysical research letters, 17(5), 575-578.

[21] Monfredini, T., Quitián-Lara, H. M., Fantuzzi, F., Wolff, W., Mendoza, E., Lago, A. F., ... & Boechat-Roberty, H. M. (2019). Destruction and multiple ionization of PAHs by X-rays in circumnuclear regions of AGNs. Monthly Notices of the Royal Astronomical Society, 488(1), 451-469.

[22] Steglich, M., Bouwman, J., Huisken, F., & Henning, T. (2011). Can neutral and ionized polycyclic aromatic hydrocarbons be carriers of the ultraviolet extinction bump and the diffuse interstellar bands?. The Astrophysical Journal, 742(1), 2.

[23] Saito, M., Sakon, I., Kaito, C., & Kimura, Y. (2010). Formation of polycyclic aromatic hydrocarbon grains using anthracene and their stability under UV irradiation. Earth, planets and space, 62, 81-90.

[24] Murri, M., Capitani, G., Fasoli, M., Monguzzi, A., Calloni, A., Bussetti, G., ... & Campione, M. (2021). Laboratory Simulation of Space Weathering on Silicate Surfaces in the Water Environment. ACS Earth and Space Chemistry, 6(1), 197-206.

[25] Mennella, V., Suhasaria, T. U. S. H. A. R., Hornekær, L., Thrower, J. D., & Mulas, G. (2021). Lyα Irradiation of Superhydrogenated Coronene Films: Implications for H2 Formation. The Astrophysical Journal Letters, 908(1), L18.

[26] Henning, T., & Salama, F. (1998). Carbon in the Universe. Science, 282(5397), 2204-2210.

[27] Malloci, G., Mulas, G., & Joblin, C. (2004). Electronic absorption spectra of PAHs up to vacuum UV-Towards a detailed model of interstellar PAH photophysics. Astronomy & Astrophysics, 426(1), 105-117.

[28] Chapman, C. R. (2004). Space weathering of asteroid surfaces. Annu. Rev. Earth Planet. Sci., 32(1), 539-567.

[29] Hendrix, A. R., & Vilas, F. (2019). C-complex asteroids: UV-visible spectral characteristics and implications for space weathering effects. Geophysical Research Letters, 46(24), 14307-14317.

[30] LASEROPTIK GmbH. (2023). *Laseroptik catalog* [PDF file]. Retrieved from https://www.laseroptik.com/data/files/Downloads/laseroptik_catalog_06-2023.pdf

[31] Hamamatsu Photonics. (2021). *D2 lamps* [Catalog]. Retrieved from https://www.hamamatsu.com/resources/pdf/etd/D2lamps_TLS1017J.pdf

[32] IRD. (2007). *IRD Catalogue* [PDF file]. Retrieved from https://file.yizimg.com/344621/2010041917431803.pdf

[33] American Scientific Glassblowers Society. (n.d.). *Optical Transmission*. Retrieved from https://asgs-glass.org/optical-transmission/